

# On the description of ductile fracture in metals by the strain localization theory

David Morin · Odd Sture Hopperstad ·

Ahmed Benallal

Received: date / Accepted: date

**Abstract** Numerical simulations based on the bifurcation and imperfection versions of the strain localization theory are used in this paper to predict the failure loci of metals and applied to an advanced high strength steel subjected to proportional loading paths. The results are evaluated against the 3D unit cell analyses of Dunand and Mohr (2014) available in the literature. The Gurson porous plasticity model (Gurson 1977) is used to induce strain softening and drive the localization process. The effects of the void growth, void nucleation and void softening in shear

---

D. Morin, O.S. Hopperstad

Centre for Advanced Structural Analysis (CASA), Norwegian University of Science and Technology (NTNU), NO-7491 Trondheim, Norway

Structural Impact Laboratory (SIMLab), Department of Structural Engineering, NTNU, NO-7491 Trondheim, Norway

E-mail: david.morin@ntnu.no

A. Benallal

LMT, ENS Paris-Saclay/CNRS/Université Paris-Saclay, 61 Avenue du Président Wilson, F-94235 Cachan, France

are investigated over a large range of stress triaxialities and Lode parameters. A correlation between the imperfection and bifurcation results is established.

**Keywords** Localization · failure · bifurcation · loss of ellipticity · porous materials

## 1 Introduction

Ductile failure in metals has been a widely studied topic in the research community during the last decades. With the emergence of new generations of high-strength steels and other advanced metals, accurate descriptions of the ductile failure process become vital in enabling the use of these materials which offer very high strength but suffer from reduced ductility. One common approach to investigate ductile failure in metals has been so far to carry out tests in a reasonably controlled manner using different types of specimens to cover a wide range of stress states (Bai and Wierzbicki 2010; Gruben et al 2011). In combination with the experimental results, detailed finite element simulations are usually conducted to determine the strain and the stress states at the location where failure is seen or supposed to initiate in the specimen. Based on this coupled experimental-numerical approach, several failure models have been proposed for ductile metals (Bai and Wierzbicki 2010; Gruben et al 2011). With the improvements of full-field measurements, Digital Image Correlation (DIC) is now routinely used to identify the parameters of existing failure models and more recently to develop new failure models (Gruben et al 2013; Jia and Bai 2016). Since ductile failure is strongly affected by load path changes (Basu and Benzerga 2015), a failure model is most commonly expressed in terms of a damage evolution rule but often based on a fracture locus valid for proportional load paths (Bai and Wierzbicki 2010; Gruben et al 2011). In

this context, the inherent drawback of physical testing is that a proportional load path is difficult to maintain up to failure initiation even if it is possible for some particular stress states (Roth and Mohr 2015). Moreover, with the variations of materials, specimen geometries, boundary conditions and measurement techniques in the literature, different conclusions can be obtained on the characteristics of ductile failure. For instance, the ductile failure strain under low stress triaxiality conditions was found to exhibit a nonmonotonic dependence to the stress triaxiality by Bai and Wierzbicki (2010) and Barsoum and Faleskog (2007), while a monotonic dependence was found by Haltom et al (2013), Ghahremaninezhad and Ravi-Chandar (2013) and Papasidero et al (2014).

While quantitative failure models require the use of physical testing, qualitative information about the mechanisms behind ductile failure can be obtained based solely on numerical simulations. With the increase in computational power over the past decade, three dimensional (3D) unit cell simulations have been successfully employed to assess the global as well as local responses of voided materials (Barsoum and Faleskog 2011; Benzerga et al 2012; Dunand and Mohr 2014; Tvergaard 2015; Bryhni Dæhli et al 2016). Based on unit cell simulations, a deeper knowledge of ductile failure has been achieved and several experimental observations have been confirmed numerically, such as the effect of the Lode parameter and the stress triaxiality on ductility (Bao and Wierzbicki 2004). In contrast to experimental tests, unit cell calculations can be carried out under fully controlled stress states which facilitate the development of failure models (Dunand and Mohr 2014). Moreover, 3D unit cell simulations can be used to study the effect of void shape and void orientation without any limitations, and void growth can be captured rather accurately as long as the matrix material is properly defined. The

---

main limitations of 3D unit cell simulations today is that the computational cost is still rather high, despite the increase in computational power, and that the quality of the local information might be influenced by the distortion of the mesh at large strains.

Very often, ductile failure is preceded by the localization of the plastic deformation within a narrow band. By assuming that the onset of localization is close to failure initiation it is therefore possible to investigate ductile failure by means of the localization theory as formulated in a quite general context by Rice (1976). Strain localization can be studied using either a bifurcation analysis or an imperfection analysis. While the bifurcation analysis has been widely used in the literature, as for instance in Besson et al (2001), Chalal and Abed-Meraim (2015) and Haddag et al (2009) in the context of ductile fracture, the imperfection analysis is less frequently used as a qualitative way of understanding ductile failure. However, some notable studies adopting the imperfection analysis to investigate strain localization are those of Yamamoto (1978), Needleman and Rice (1979), Hutchinson and Tvergaard (1981), Saje et al (1982), Mear and Hutchinson (1985), Nahshon and Hutchinson (2008) and Gruben et al (2017). To trigger localization in a material at reasonable stresses, a softening mechanism must be present in the constitutive equations of the material (Rudnicki and Rice 1975) when the inelastic flow is associative as commonly assumed for metals that are investigated here. A natural way to include strain softening into the constitutive description for ductile fracture is to consider a porous plasticity model, such as the Gurson model (Gurson 1977), where a voided material is modelled. In this perspective, the main limitation of the present study is the mathematical formulation of the porous plasticity model, which is based on different types of assumptions. As a

consequence, the conclusions to be drawn from the analysis are probably dependent on the adopted formulation but one can also expect some general qualitative conclusions. This weakness is balanced to some extent by the CPU efficiency of localization analyses, which allows to investigate a wide range of stress states in a limited amount of time. With the continuous improvements of the porous plasticity models, e.g Madou and Leblond (2012), Morin et al (2016) and Benallal (2017) it is expected that this weakness will be reduced.

In this study, strain localization simulations by means of the imperfection analysis proposed by Rice (1976) are employed to predict the failure locus under proportional loading and to gain insight into the processes leading to ductile failure. In order to allow for strain softening and thus trigger strain localization, the Gurson model is applied to describe the behaviour of the material, including growth, nucleation and void softening in shear. To assess the adopted approach, comparisons are made with the results from 3D unit cell simulations presented by Dunand and Mohr (2014). The influence of the various parameters of the Gurson model on the predicted failure locus is evaluated in a sensitivity study. The results of the imperfection analysis are finally investigated from the band perspective and compared to those of the bifurcation analysis leading to some important conclusions.

The outline of the paper is as follows. Section 2 briefly reviews the theory of localization in its bifurcation and imperfection versions. Section 3 describes the porous plasticity model used to trigger localization, namely the Gurson model with its different improvements and extensions to include beside void growth, nucleation and void softening in shear. The parameter identification and selection is given in Section 4, while Section 5 contains the numerical implementation of both approaches. The numerical results for the imperfection analysis are given in

Section 6 where they are compared to the 3D cell simulations of Dunand and Mohr (2014). Section 7 is dedicated to a deeper analysis of the imperfection approach and the localization process occurring in the band. On the basis of these results, a link is also established between the imperfection and bifurcation approaches. Conclusions are provided in Section 8.

## 2 Localization analysis

In their investigation on localization in plastically dilatant materials with pressure sensitive yielding, Rudnicki and Rice (1975) through the use of a bifurcation analysis on a perfect material have clearly shown that localization necessitates strongly negative plastic moduli in the case of axially-symmetric extension or compression. In order to assess the effects of non-uniformities in the localization process, Rice (1976) has proposed a formulation in the spirit of the Marciniak-Kuczynski analysis in local necking of thin metal sheets (Marciniak and Kuczynski 1967). This idea allows localization and failure to take place for lower strains than the ones required for a perfectly homogeneous body, as shown by Yamamoto (1978) and Needleman and Rice (1979) later. This is explained by the fact that a part of a material that has slightly different properties from the remaining portion concentrates deformation within this inhomogeneity (imperfection).

In the imperfection analysis, we consider a homogeneously deformed body in which a thin planar band with a small imperfection is present (Rice 1976). The stress and strain rates as well as the constitutive relations inside the band are allowed to be different from those outside the band, but equilibrium and compatibility across the band are enforced. Taking the reference configuration to coincide

momentarily with the current configuration, the equations for continuing equilibrium are expressed as

$$\mathbf{n} \cdot \dot{\mathbf{P}}_b = \mathbf{n} \cdot \dot{\mathbf{P}} \quad (1)$$

where  $\mathbf{n}$  is the normal to the band and  $\mathbf{P}$  is the nominal stress tensor. The subscript  $b$  denotes a quantity inside the band. Furthermore, the rate of the nominal stress tensor  $\dot{\mathbf{P}}$  is then given by

$$\dot{\mathbf{P}} = \dot{\boldsymbol{\sigma}} - \mathbf{L} \cdot \boldsymbol{\sigma} + (\mathbf{D} : \mathbf{I}) \boldsymbol{\sigma} \quad (2)$$

where  $\boldsymbol{\sigma}$  is the Cauchy stress tensor,  $\mathbf{L}$  is the velocity gradient tensor,  $\mathbf{D} = \frac{1}{2}(\mathbf{L} + \mathbf{L}^T)$  is the rate-of-deformation tensor, and  $\mathbf{I}$  is the second-order identity tensor. The relation between the band normals  $\mathbf{n}_0$  and  $\mathbf{n}$  in the initial and current configurations, respectively, is given by Needleman and Rice (1979)

$$\mathbf{n} = \frac{\mathbf{n}_0 \cdot \mathbf{F}^{-1}}{\|\mathbf{n}_0 \cdot \mathbf{F}^{-1}\|} \quad (3)$$

where  $\mathbf{F}$  is the deformation gradient of the material outside the band. The deformation gradient  $\mathbf{F}$  maps the initial (undeformed) configuration into the current configuration. Compatibility implies that the velocity gradient field can only vary along the normal direction of the planar band and thus

$$\mathbf{L}_b = \mathbf{L} + \dot{\mathbf{q}} \otimes \mathbf{n} \quad (4)$$

where  $\dot{\mathbf{q}}$  is a vector that represents the rate-of-deformation non-uniformity. The unit vector  $\mathbf{m} = \dot{\mathbf{q}}/\|\dot{\mathbf{q}}\|$  determines the localization mode. If  $\mathbf{m} \cdot \mathbf{n} = 0$ , a shear band is obtained, while if  $\mathbf{m} \cdot \mathbf{n} = 1$ , the band is a dilatation band. A mixed type of localization mode is obtained in all other cases.

Assuming rate-independent plasticity and using a formulation in terms of the Jaumann stress rate, the rate constitutive equations may be expressed as

$$\dot{\boldsymbol{\sigma}} = \mathbf{C}^{ep} : \mathbf{D} + \mathbf{W} \cdot \boldsymbol{\sigma} + \boldsymbol{\sigma} \cdot \mathbf{W}^T \quad (5)$$

where  $\mathbf{C}^{ep}$  is the elastic-plastic tangent modulus tensor, assumed to exhibit the minor and major symmetries, and  $\mathbf{W} = \frac{1}{2}(\mathbf{L} - \mathbf{L}^T)$  is the spin tensor. Using Equation (2), we get the alternative form

$$\dot{\mathbf{P}} = \mathbf{C}^{ep} : \mathbf{D} + \boldsymbol{\sigma} \cdot \mathbf{W}^T - \mathbf{D} \cdot \boldsymbol{\sigma} + (\mathbf{D} : \mathbf{I}) \boldsymbol{\sigma} \quad (6)$$

which becomes after some rearrangements

$$\dot{\mathbf{P}} = \mathbf{C}^t : \mathbf{L} \quad (7)$$

where the tangent modulus tensor  $\mathbf{C}^t$  is given by

$$C_{ijkl}^t = C_{ijkl}^{ep} - \frac{1}{2}\sigma_{ik}\delta_{jl} + \frac{1}{2}\sigma_{il}\delta_{kj} - \frac{1}{2}\sigma_{jl}\delta_{ik} - \frac{1}{2}\sigma_{jk}\delta_{il} + \sigma_{ij}\delta_{kl} \quad (8)$$

where  $\delta_{ij}$  is the Kronecker delta. A similar rate constitutive equation holds for the material inside the band with the subscript  $b$  is attached to all quantities inside the band.

By combining Equations (1), (4) and (7), an equation for the rate-of-deformation non-uniformity  $\dot{\mathbf{q}}$  is obtained as

$$(\mathbf{n} \cdot \mathbf{C}_b^t \cdot \mathbf{n}) \cdot \dot{\mathbf{q}} = \mathbf{n} \cdot (\mathbf{C}^t - \mathbf{C}_b^t) : \mathbf{L} \quad (9)$$

where  $\mathbf{C}_b^t$  is the tangent modulus tensor inside the band. Loss of ellipticity, or strain localization, occurs when the acoustic tensor  $\mathbf{A}^t(\mathbf{n}) = \mathbf{n} \cdot \mathbf{C}_b^t \cdot \mathbf{n}$  becomes singular, viz.

$$\det(\mathbf{n} \cdot \mathbf{C}_b^t \cdot \mathbf{n}) = 0 \quad (10)$$

For materials undergoing associative plastic flow, this condition is not met unless strain softening is present in the constitutive response of the material in the imperfection band (except for large stresses with no practical interest for metals). Strain softening in ductile metals is often linked to damage evolution and/or thermal softening. In this study, the Gurson model (Gurson 1977) for porous plasticity is adopted for the material behaviour inside the band, thus to describe strain softening due to void growth and eventually loss of ellipticity. But any other mechanism that is observable for real materials and leading to softening can be considered.

In the bifurcation analysis, we consider a homogeneous and homogeneously deformed body which is subjected to a uniform stress or velocity gradient field and investigate the possibility of a bifurcation. Specifically, following Rice (1976), we search for conditions "for which continued deformation may result in an incipient non-uniform field in which deformation rates vary with position across a planar band but remain uniform outside the band". The condition for bifurcation is obtained from Equation (10) by setting  $\mathbf{C}_b^t = \mathbf{C}^t$  and, accordingly, the bifurcation condition is met when the acoustic tensor  $\mathbf{A}^t$  of the homogeneous material becomes singular. Loss of ellipticity, as for the imperfection analysis, can only be obtained by including strain softening when associative plastic flow is assumed in the elastic-plastic constitutive equations.

### 3 Porous plasticity

Strain softening in ductile metals is often linked to damage evolution and/or adiabatic heating. If the latter is dismissed when considering quasi-static loading

conditions, damage evolution can be captured by using a micromechanical-based porous plasticity model, such as the Gurson model (Gurson 1977). This porous plasticity model is rather appealing due to its limited number of parameters. In this study, a hypoelastic-plastic formulation of the Gurson model is employed in the localization analysis.

The additive decomposition of the rate-of-deformation tensor  $\mathbf{D}$  is assumed, viz.

$$\mathbf{D} = \mathbf{D}^e + \mathbf{D}^p \quad (11)$$

where  $\mathbf{D}^e$  is the elastic part of the rate-of-deformation tensor and  $\mathbf{D}^p$  is its plastic counterpart. The hypoelastic relation is defined by

$$\dot{\boldsymbol{\sigma}} = \mathbf{C} : \mathbf{D}^e + \mathbf{W} \cdot \boldsymbol{\sigma} + \boldsymbol{\sigma} \cdot \mathbf{W}^T \quad (12)$$

where  $\mathbf{C}$  is the elasticity tensor. Isotropic elasticity is assumed here and  $\mathbf{C}$  depends only on Young's modulus  $E$  and Poisson's ratio  $\nu$ .

The Gurson yield function, as modified by Tvergaard (1981), reads as

$$\Phi = \left( \frac{\varphi(\boldsymbol{\sigma})}{\sigma_M} \right)^2 + 2q_1 f \cosh \left( \frac{q_2}{2} \frac{\boldsymbol{\sigma} : \mathbf{I}}{\sigma_M} \right) - (1 + q_3 f^2) \quad (13)$$

where  $\sigma_{eq} \equiv \varphi(\boldsymbol{\sigma}) = \sqrt{\frac{3}{2} \boldsymbol{\sigma}' : \boldsymbol{\sigma}'}$  is the equivalent stress,  $\boldsymbol{\sigma}'$  is the deviatoric part of the Cauchy stress tensor,  $\sigma_M$  is the flow stress of the matrix,  $f$  the porosity, and  $q_1$ ,  $q_2$  and  $q_3$  are parameters introduced by Tvergaard (1981). The associative flow rule is assumed and the plastic rate-of-deformation tensor  $\mathbf{D}^p$  is therefore defined as

$$\mathbf{D}^p = \dot{\lambda} \frac{\partial \Phi}{\partial \boldsymbol{\sigma}} \quad (14)$$

where  $\dot{\lambda}$  is the plastic parameter. The loading-unloading conditions are stated in their Kuhn-Tucker form

$$\Phi \leq 0, \quad \dot{\lambda} \geq 0, \quad \dot{\lambda} \Phi = 0 \quad (15)$$

while  $\dot{\lambda}$  is obtained from the consistency condition and  $\dot{\Phi} = 0$  when  $\dot{\lambda}$  is positive.

The work hardening of the matrix material is described by a three-term Voce rule in the form

$$\sigma_M = \sigma_0 + \sum_{i=1}^3 Q_i \left( 1 - \exp \left( -\frac{\theta_i}{Q_i} p \right) \right) \quad (16)$$

where  $\sigma_0$  is the initial yield stress,  $Q_i$  and  $\theta_i$  are the saturation stress and initial work hardening modulus of the  $i^{th}$  hardening term. The equivalent plastic strain  $p$  of the matrix material is defined as

$$p = \int \dot{p} dt = \int \frac{\boldsymbol{\sigma} : \mathbf{D}^p}{(1-f)\sigma_M} dt \quad (17)$$

When using the Gurson model to describe strain softening, the porosity  $f$  requires an initial value  $f_0$  as well as an evolution rule. In the literature, the void evolution rule is frequently decomposed as

$$\dot{f} = \dot{f}_g + \dot{f}_n + \dot{f}_s \quad (18)$$

where  $\dot{f}_g$  is the void growth rate,  $\dot{f}_n$  is the void nucleation rate, and  $\dot{f}_s$  represents the contribution of void softening in shear (not present in the original Gurson model) to the porosity evolution. Assuming an incompressible matrix material, the void growth rate  $\dot{f}_g$  is linked to the volumetric plastic strain rate as

$$\dot{f}_g = (1-f) \mathbf{D}^p : \mathbf{I} \quad (19)$$

When nucleation of voids is taken into account in this study, the void nucleation rate  $\dot{f}_n$  is assumed to be strain driven and expressed as (Chu and Needleman 1980)

$$\dot{f}_n = \mathcal{A} \dot{p} \quad (20)$$

where

$$\mathcal{A} = \frac{f_n}{s_n \sqrt{2\pi}} \exp \left[ -\frac{1}{2} \left( \frac{p - p_n}{s_n} \right)^2 \right] \quad (21)$$

Here,  $f_n$  is the volume fraction of void nucleating particles,  $p_n$  is the mean equivalent plastic strain for nucleation, and  $s_n$  is the associated standard deviation. The original Gurson model does not describe strain softening for low stress triaxialities, as for example in shear-dominated stress states. To overcome this problem, Nahshon and Hutchinson (2008) proposed a phenomenological extension of the Gurson model in which damage growth is invoked under low stress triaxiality to account for shear softening due to void distortion and inter-void linking. When applied in this study, its contribution to the porosity evolution

$$\dot{f}_s = k_s f \kappa(\boldsymbol{\sigma}') \frac{\boldsymbol{\sigma}' : \mathbf{D}^p}{\varphi(\boldsymbol{\sigma})} \quad (22)$$

where  $k_s$  is a constant and  $\kappa(\boldsymbol{\sigma}')$  is a function of the second and third invariant of the deviatoric stress tensor,  $J_2 = \frac{1}{2} \boldsymbol{\sigma}' : \boldsymbol{\sigma}'$  and  $J_3 = \det(\boldsymbol{\sigma}')$ , respectively, viz.

$$\kappa(\boldsymbol{\sigma}') = 1 - \frac{27}{4} \frac{J_3^2}{J_2^3} \quad (23)$$

As pointed out by Nahshon and Hutchinson (2008), when the void softening in shear is contributing to the void evolution (Equation 18), the void content  $f$  loses its physical meaning and should be interpreted as a damage parameter. However, in this study this distinction is not made when discussing the results linked to the porous plasticity model.

The Gurson model is implemented into a standalone FORTRAN programme. The stress update algorithm proposed by Aravas (1987) is adopted due to its robustness and cost efficiency.

#### 4 Material parameters

The material parameters are determined based on the data for a TRIP steel provided by Dunand and Mohr (2014). The behaviour of the material is defined by the elastic constants, the initial yield stress and the hardening parameters, as well as the parameters governing initial porosity and porosity evolution.

The elastic constants, namely Young's modulus  $E$  and Poisson's ratio  $\nu$ , are given the typical values of steel (see Table 1). The initial yield stress  $\sigma_0$  and work hardening parameters  $Q_i$  and  $\theta_i$  ( $i = 1, 2, 3$ ) are obtained by a least-square fitting of Equation (16) to the data reported by Dunand and Mohr (2014). An illustration of the obtained fit is shown in Figure 1 along with the correlation factor  $R^2$ . The parameter values are given in Table 1.

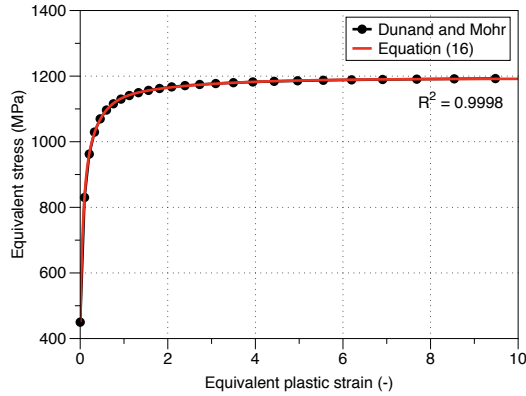


**Fig. 1** Strain hardening curve for the TRIP steel used in the simulations. The extended Voce hardening rule given in Equation (16) is compared with data provided in Dunand and Mohr (2014).

Dunand and Mohr (2014) carried out their unit cell analyses with an initially spherical void representing 0.7% of the volume of the unit cell. Therefore, the ini-

$E_0$ (MPa)	$\nu$	$\sigma_0$ (MPa)	$\theta_1$ (MPa)	$Q_1$ (MPa)
210000	0.3	450.0	6010.0	371.4
$\theta_2$ (MPa)	$Q_2$ (MPa)	$\theta_3$ (MPa)	$Q_3$ (MPa)	
987.9	291.7	42.16	78.95	

**Table 1** Material parameters for the elastic and plastic behaviour of the TRIP steel.

tial porosity  $f_0$  of the porous plasticity model is set equal to 0.7 %. The parameters governing the void nucleation and the void softening in shear cannot be estimated from the unit cell analyses and their influences are therefore examined in a sensitivity study. While the imperfection analysis allows us to include porosity both inside and outside the band, porosity is introduced only inside the imperfection band in this study. Thus, the porosity is initially zero and remains zero outside the band, whereas inside the band the porosity evolves and may eventually lead to strain softening and localization there. Note here that the Gurson yield function is reduced to the von Mises yield function for zero initial porosity, and in absence of void nucleation, the porosity remains equal to zero during plastic straining.

## 5 Numerical implementation

### 5.1 Imperfection analysis

The imperfection analysis is performed by prescribing a proportional load path outside the band and then computing the response of the band material so that continuing equilibrium and compatibility equations are satisfied at each time step. The Gurson model is used to describe the material behaviour with non-zero porosity inside the band and zero porosity outside it (thus reducing to a von Mises

material). Localization is assumed to occur when the determinant of the acoustic tensor becomes slightly negative for the first time. To find the critical band orientation, a large number of band orientations is investigated for each prescribed load path.

The band orientation is defined by the unit normal to the band in the initial (undeformed) configuration  $\mathbf{n}_0$ , which in the global Cartesian coordinate system  $(X_1, X_2, X_3)$  (see Figure 2) is defined as

$$\mathbf{n}_0 = \begin{Bmatrix} \cos \phi_0 \\ \cos \theta_0 \sin \phi_0 \\ \sin \theta_0 \sin \phi_0 \end{Bmatrix} \quad (24)$$

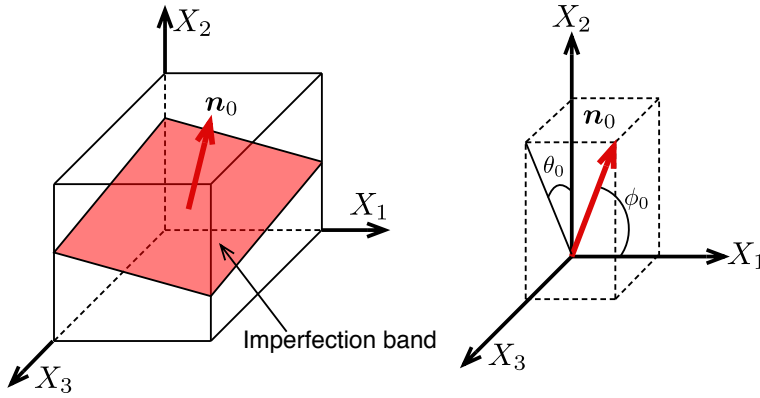


**Fig. 2** Representation of the imperfection band with its orientation in the initial (undeformed) configuration.

In the current configuration, at time  $t$ , the band orientation (or more precisely the band normal) is calculated according to

$$\mathbf{n}(t) = \frac{\mathbf{n}_0 \cdot \mathbf{F}^{-1}(t)}{\|\mathbf{n}_0 \cdot \mathbf{F}^{-1}(t)\|} \quad (25)$$

where  $\mathbf{F}(t)$  is the deformation gradient outside the band. The inverse deformation gradient is computed using the velocity gradient  $\mathbf{L}(t)$  according to

$$\mathbf{F}^{-1}(t) = [\mathbf{I} - \Delta t \mathbf{L}(t)] \cdot \mathbf{F}^{-1}(t - \Delta t) \quad (26)$$

where  $\Delta t$  is the current time step. In the imperfection analysis, loss of ellipticity can occur for several band orientations (Mear and Hutchinson 1985; Nahshon and Hutchinson 2008), but only one band will lead to the lowest ductility. It is therefore important to search within a broad range of initial orientations for this critical band. The procedure to find the critical band orientation is detailed at the end of this paragraph, while the applied computational scheme for an arbitrary band orientation is presented in the following.

The loading path outside the band is defined so as to ensure proportional loading defined by the stress triaxiality  $T$  and the Lode parameter  $L$ , defined by

$$T = \frac{1}{3} \frac{\boldsymbol{\sigma} : \mathbf{I}}{\sigma_{eq}}, \quad L = \frac{2\sigma_2 - \sigma_1 - \sigma_3}{\sigma_1 - \sigma_3} \quad (27)$$

where  $\sigma_1, \sigma_2$  and  $\sigma_3$  are the ordered principal stresses,  $\sigma_1 \geq \sigma_2 \geq \sigma_3$ . To this end, the stress tensor outside the band is taken as

$$\boldsymbol{\sigma}(t) = \xi(t) \bar{\boldsymbol{\sigma}} \quad (28)$$

where  $\xi(t)$  is a dimensionless loading parameter and  $\bar{\boldsymbol{\sigma}}$  represents a fixed reference stress state which is defined by  $T$  and  $L$ . The principal reference stresses are defined as

$$\begin{Bmatrix} \bar{\sigma}_1 \\ \bar{\sigma}_2 \\ \bar{\sigma}_3 \end{Bmatrix} = \sigma_0 \left[ \frac{2}{3} \begin{Bmatrix} \cos \theta_L \\ \cos(\theta_L - \frac{2\pi}{3}) \\ \cos(\theta_L + \frac{2\pi}{3}) \end{Bmatrix} + T \begin{Bmatrix} 1 \\ 1 \\ 1 \end{Bmatrix} \right] \quad (29)$$

where  $\sigma_0$  is the yield stress (used here as a scaling factor) and  $\theta_L$  is the Lode angle, which is defined as

$$\cos(3\theta_L) = \frac{J_3}{2} \left( \frac{3}{J_2} \right)^{\frac{3}{2}} \quad (30)$$

where  $\theta_L \in [0, \pi/6]$ . The Lode angle  $\theta_L$  is  $0^\circ$  for  $L = -1$ ,  $30^\circ$  for  $L = 0$  and  $60^\circ$  for  $L = 1$ . This procedure implies that the principal stress directions are fixed outside the band and coincide with the global Cartesian coordinate system  $(X_1, X_2, X_3)$ .

Since the spin is taken to be zero outside the band,  $\mathbf{W} = 0$ , we have  $\mathbf{L} = \mathbf{D}$  and Equation (28) leads to the incremental update

$$\Delta\boldsymbol{\sigma}(t) = \Delta\xi(t)\bar{\boldsymbol{\sigma}} = \mathbf{C}^{ep}(t - \Delta t) : \Delta\boldsymbol{\varepsilon}(t) \quad (31)$$

where  $\Delta\boldsymbol{\varepsilon}(t) = \mathbf{D}(t)\Delta t$ . Solving for  $\Delta\boldsymbol{\varepsilon}(t)$ , we get

$$\Delta\boldsymbol{\varepsilon}(t) = \Delta\xi(t) (\mathbf{C}^{ep}(t - \Delta t))^{-1} : \bar{\boldsymbol{\sigma}} \quad (32)$$

where  $\Delta\xi(t)$  is adjusted to get a prescribed magnitude  $\Delta\varepsilon(t) = \|\Delta\boldsymbol{\varepsilon}(t)\|$  of the incremental strain tensor at time  $t$ . The norm of the incremental strain tensor is here defined as  $\|\Delta\boldsymbol{\varepsilon}(t)\| = \sqrt{\Delta\boldsymbol{\varepsilon}(t) : \Delta\boldsymbol{\varepsilon}(t)}$ . As this procedure is explicit in nature, relatively small strain increments are required to enforce the prescribed proportional load path. With  $\Delta\boldsymbol{\varepsilon}(t)$  determined by Equation (32), the material outside the band is then deformed up to very large strains for a given proportional load path, and the velocity gradient  $\mathbf{L}(t)$  and the tangent modulus tensor  $\mathbf{C}^t(t)$  are stored at each time step for later use in the localization analysis.

For a given proportional loading path  $(T, L)$  and an initial band orientation  $\mathbf{n}_0$ , the velocity gradient inside the band  $\mathbf{L}_b$  is calculated, according to Equation (4), as

$$\Delta t \mathbf{L}_b(t) = \Delta\boldsymbol{\varepsilon}(t) + \Delta\mathbf{q}(t) \otimes \mathbf{n}(t) \quad (33)$$

with  $\Delta\mathbf{q}(t) = \Delta t \dot{\mathbf{q}}(t)$ , and then used to calculate the tangent modulus tensor  $\mathbf{C}_b^t(t)$  inside the band. In the above equation,  $\Delta\mathbf{q}(t)$  is unknown and is determined with a fixed point iteration method using  $\Delta\mathbf{q}(t - \Delta t)$  as the initial value. An improved estimate of  $\Delta\mathbf{q}(t)$  is then obtained from the residual form of Equation (10), viz.

$$\mathbf{R}(t) = \mathbf{A}^t(t) \cdot \Delta\mathbf{q}(t) - \mathbf{B}(t) = \mathbf{0} \quad (34)$$

where

$$\mathbf{A}^t(t) = \mathbf{n}(t) \cdot \mathbf{C}_b^t(t) \cdot \mathbf{n}(t) \quad (35)$$

$$\mathbf{B}(t) = \mathbf{n}(t) \cdot \left( \mathbf{C}^t(t) - \mathbf{C}_b^t(t) \right) : \Delta\boldsymbol{\varepsilon}(t) \quad (36)$$

Next, the updated value of  $\Delta\mathbf{q}(t)$  is inserted into Equation (33) and the tensors  $\mathbf{L}_b(t)$  and  $\mathbf{C}_b^t(t)$  inside the band are updated accordingly. Convergence is assumed when the ratio  $\|\mathbf{R}\|/\sigma_0$  is less than a given tolerance.

The proposed computational scheme will experience difficulties in enforcing equilibrium when ellipticity is lost, as the problem becomes ill-posed. To avoid such numerical instabilities, the determinant of the acoustic tensor  $\det \mathbf{A}^t(t)$  is computed before initiating a new iteration and loss of ellipticity is detected when this quantity becomes negative. While the condition expressed in Equation (10) is the stringent condition for loss of ellipticity, it is difficult to satisfy it exactly within a numerical framework. Loss of ellipticity is therefore assumed to occur for the first negative value of  $\det \mathbf{A}^t(t)$ , and, thus, when a negative value is detected, the time incrementation is stopped. As stated in the beginning of this paragraph, loss of ellipticity may be detected for several band orientations and it is important to find the most critical orientation, i.e., the orientation for which the ductility is smallest. As found by means of imperfection analysis in (Mear and Hutchinson 1985; Nahshon and Hutchinson 2008) and unit cell simulations in (Dunand and

Mohr 2014; Barsoum and Faleskog 2011), the failure strain is a convex function of the initial orientation of the band. It is considered here that localization takes place within a planar band with normal in the plane defined by the major and minor principal stress directions, as remarked by Rudnicki and Rice (1975). The conditions for which this result holds are given in Benallal and Comi (1996) for general constitutive equations within the small strain assumption. Corotational terms will not change these results for materials like metals considered here. This fact is also adopted in the cell calculations of Dunand and Mohr (2014) to which our results will be compared. Accordingly, the band normal  $\mathbf{n}_0$  can be expressed in the global Cartesian coordinate system  $(X_1, X_2, X_3)$  as

$$\mathbf{n}_0 = \begin{Bmatrix} \cos \phi_0 \\ 0 \\ \sin \phi_0 \end{Bmatrix} \quad (37)$$

where  $\phi_0$  is the angle between the band normal and the  $X_1$ -axis. This allows us to characterize the localization bands by a single angle, either  $\phi_0$  in the initial configuration or  $\phi$  in the current configuration. As a result, it is possible to search for the most critical band using an iterative procedure with domain reduction. A graphical illustration of this method is given in Figure 3. In iteration  $i$ , a set of 11 bands is distributed in the search domain of  $\phi_0 \in [0^\circ, 90^\circ]$  and the localization analysis is carried out for each of these orientations until loss of ellipticity is detected for one of them. At iteration  $i + 1$  the eleven orientations are distributed between the orientations bounding the critical one in iteration  $i$ . This operation is repeated until the equivalent plastic strain at localization in the material outside the band has converged within a given tolerance.

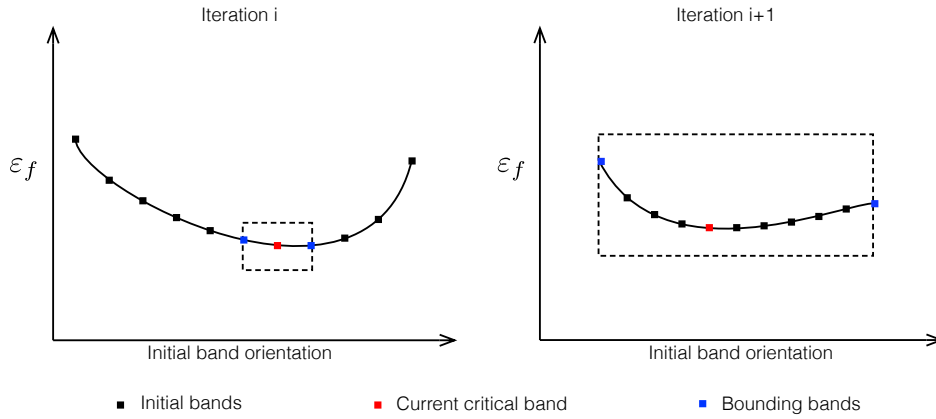


**Fig. 3** Schematic description of the optimization procedure used to determine the critical band orientation.

## 5.2 Bifurcation analysis

A similar approach as described in the previous section, is also used in the bifurcation analysis. First, the material is deformed until very large strains using the Gurson model and then bifurcation is sought for within a set of band orientations. Recall that bifurcation is only possible when the material exhibits strain softening, and there is no need to search for localization in the hardening region of deformation. The maximum deformation the material can sustain occurs at the strain which gives a porosity  $f$  equal to  $0.9q_1^{-1}$ , with the underlying assumption that  $q_3 = q_1^2$ . The material is then loaded incrementally up to this maximum strain by keeping the stress triaxiality  $T$  and the Lode parameter  $L$  constant, using the same method as explained above. The tangent modulus tensor  $\mathbf{C}^t(t)$  of the material is then extracted and used in the bifurcation analysis.

The condition for bifurcation, or loss of ellipticity, is given by

$$\det(\mathbf{A}^t(t)) = \det(\mathbf{n}(t) \cdot \mathbf{C}^t(t) \cdot \mathbf{n}(t)) = 0 \quad (38)$$

As for the imperfection analysis, the first instant where the determinant of the acoustic tensor becomes negative is assumed to be the point of bifurcation.

In order to find the critical orientation of the localization band in the softening regime, a set of potential band orientations is checked for localization. The band normal  $\mathbf{n}$  in the current configuration is defined in the global Cartesian coordinate system  $(X_1, X_2, X_3)$  as

$$\mathbf{n} = \begin{Bmatrix} \cos \phi \\ 0 \\ \sin \phi \end{Bmatrix} \quad (39)$$

where  $\phi$  is the angle between the band normal and the  $X_1$ -axis. The band orientations investigated are in the domain  $\phi \in [0^\circ, 90^\circ]$ . The sequential method with domain reduction is also applied here to determine the critical band orientation yielding the smallest ductility. The bifurcation analysis is significantly less CPU time consuming because we do not have to follow the evolution of a set of imperfection bands from the initial configuration until localization occurs in one of them.

## 6 Numerical study

### 6.1 Preamble

The strain localization analysis with the imperfection approach will be compared to the localization analysis carried out by Dunand and Mohr (2014) using 3D unit cell simulations. A large range of stress states is investigated here using the previously described algorithm. The stress triaxiality  $T$  ranges from 0 to 4 and the Lode parameter  $L$  varies between -1 and 1. A total of 1600 different stress

states are used. The sequential method with domain reduction investigates, in average, 30 band orientations per stress state, and, in average, three iterations are required to obtain a converged failure strain  $\varepsilon_f$  with a tolerance of  $\pm 1e^{-4}$ . The proposed computational strategy leads to a run time below 10 minutes for the 1600 stress states on a Linux cluster equipped with 48 Intel Xeon X5650 processors. According to Dunand and Mohr (2014), one unit cell analysis for a particular stress state has a run time of 3 hours. This average computational time would lead to a total computation time of approximately 17 years using 3D unit cell analyses to cover the same range of stress states. The very good computational efficiency of the localization imperfection analysis makes this technique worth investigating to obtain qualitative knowledge on ductile failure.

All quantities used in this section are extracted from *the material outside the band* when localization is detected in the critical imperfection band. Thus, the failure strain  $\varepsilon_f$  is defined as the equivalent plastic strain  $p$  from the material outside the band and is obtained through Equation (17) with  $f = 0$ .

## 6.2 Effect of porous plasticity parameters

As already mentioned, the imperfection analysis relies on the quality of the porous plasticity model used to describe damage evolution and strain softening inside the band. To evaluate the effect of the porous plasticity model, the Gurson model is used first with porosity evolution based only on growth of pre-existing voids, i.e., both nucleation and void softening in shear are neglected, while the parameters  $q_1$ ,  $q_2$  and  $q_3$  are varied. Figure 4 shows the effect of these parameters on the failure strain obtained with the imperfection analysis and how the results compare

with those reported by Dunand and Mohr (2014). Results are shown for stress triaxialities  $T = 0.2, 0.5$  and  $1.0$  and with the Lode parameter  $L$  varied between  $-1$  and  $1$ . Three sets of porous plasticity parameters are considered:

- $q_1 = q_2 = q_3 = 1.0$  corresponding to the original Gurson model (Gurson 1977),
- $q_1 = 1.5, q_2 = 1.0, q_3 = q_1^2$  corresponding to parameters proposed by Tvergaard (1981),
- $q_1 = 1.86, q_2 = 0.74, q_3 = q_1^2$  corresponding to parameters used by Faleskog et al (1998).

From Figure 4 it is first interesting to note that independently from the values of the parameters  $q_1, q_2$  and  $q_3$ , a similar shape of the failure locus is obtained. The imperfection analysis predicts a global dependence of the failure strain on both stress triaxiality and Lode parameter just as the 3D unit cells from Dunand and Mohr (2014). While the dependence on the stress triaxiality should be expected, because the Gurson model depends on the first invariant of the stress tensor, the dependence on the Lode parameter is a result of the localization phenomenon. The intrinsic Lode parameter dependency is in accordance with the findings of Rudnicki and Rudnicki and Rice (1975) (while the Lode parameter  $L$  was not explicitly mentioned). Asymmetric convex failure loci with respect to the Lode parameter are obtained with the imperfection analysis, giving a higher ductility for generalized compression ( $L = 1$ ) than for generalized tension ( $L = -1$ ). The lowest failure strain is typically found close to generalized shear ( $L = 0$ ) for the presented stress triaxialities. With the original Gurson model ( $q_1 = q_2 = q_3 = 1.0$ ), strain localization was not obtained within the investigated strain range  $0 \leq \|\boldsymbol{\varepsilon}(t)\| \leq 3$  for stress triaxialities less than or equal to  $0.2$ . While the shape of the failure locus

is correct for  $T = 0.5$  and 1 with this set of parameters, the magnitude of the failure strain is strongly overestimated. The hardening parameters used in this study are representative for a TRIP steel, which exhibits a strong work-hardening even at large strains (Dunand and Mohr 2014). As void growth is influenced by the work-hardening of the surrounding matrix, the original Gurson model ( $q_1 = q_2 = q_3 = 1.0$ ) is deemed not to be an appropriate choice for this material.

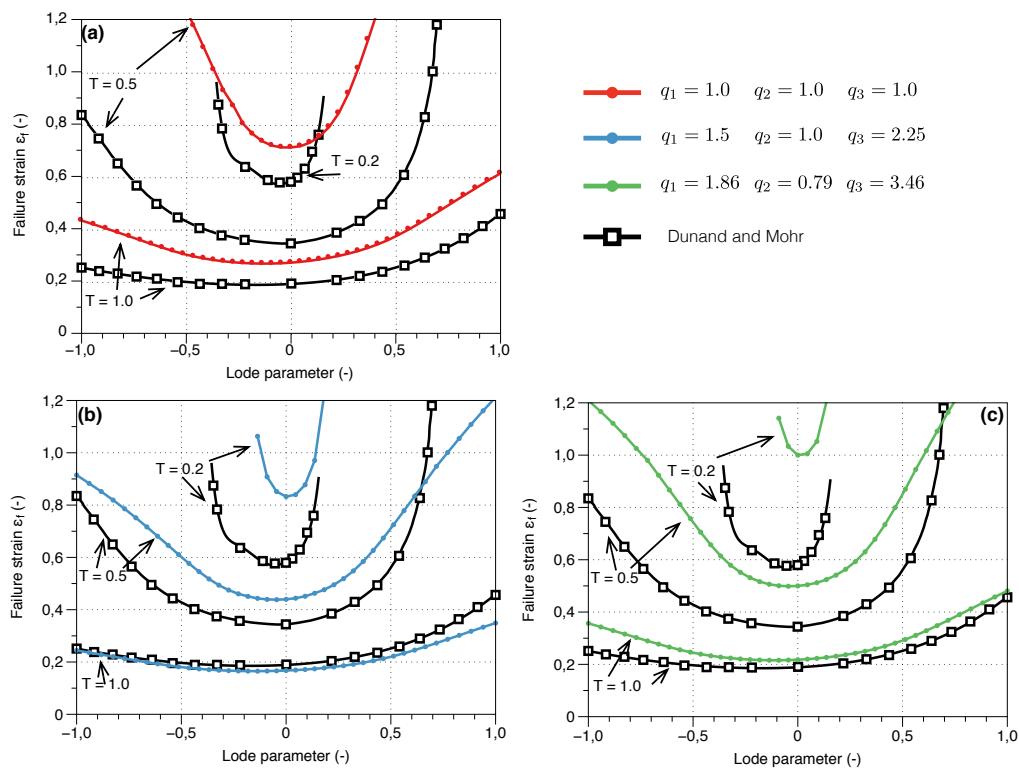


**Fig. 4** Effect of the porous plasticity parameters  $q_1$ ,  $q_2$  and  $q_3$  on the failure locus: a) original Gurson model, b) parameters from Tvergaard (1981) and c) parameters from Faleskog et al (1998)

While the shape of the failure locus and magnitude of the failure strains at a stress triaxiality  $T$  equal to 1 seem to be captured rather well by the parameters proposed by Tvergaard (1981) and Faleskog et al (1998), the failure strains are still strongly overestimated at low triaxiality ( $T = 0.2$ ). At high stress triaxiality the hypothesis of spherical void growth is most likely correct and the good agreement between the localization analyses and the unit cell simulations might be expected. As stated in several studies, at low stress triaxialities the void growth is no longer spherical and the original Gurson model is then failing to describe the proper void shape and potential growth of the void. This results in the overestimation of the failure strains in the localization analyses compared with the unit cell simulations.

It is concluded, in the light of the obtained results here that none of the three sets of parameters is able to reproduce all of the 3D unit cell results. In the regime of low stress triaxialities, as already documented in the literature (Nahshon and Hutchinson 2008), other mechanisms should be included and are the subjects of the next two sections.

### 6.3 Effect of the void softening in shear

In this section, the effect of possible void softening in shear is analysed using the shear modification proposed by Nahshon and Hutchinson (2008). The porous plasticity parameters  $q_1$ ,  $q_2$  and  $q_3$  are here fixed to be those proposed by Tvergaard (1981) since they offer the best agreement with the unit cell results. The parameter  $k_s$  is varied from 1 to 3 (as proposed by Nahshon and Hutchinson (2008)) and the obtained results are compared to those obtained with the Gurson model without void softening in shear ( $k_s = 0$ ).

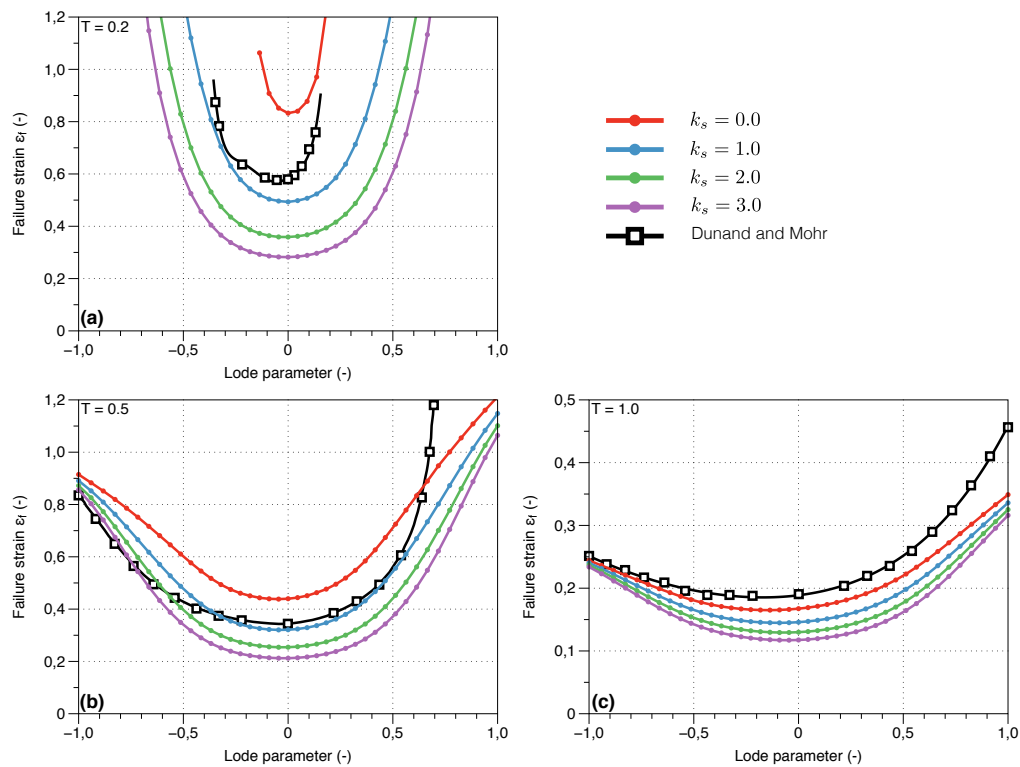


**Fig. 5** Effect of void softening in shear on the failure locus at different stress triaxialities: a)  $T = 0.2$ , b)  $T = 0.5$  and c)  $T = 1.0$ .

The resulting failure strains are reported in Figure 5 a), b) and c) for stress triaxiality  $T = 0.2, 0.5$  and  $1$ , respectively. As also demonstrated in (Nahshon and Hutchinson 2008), introducing the effect of void softening in shear into the Gurson model allows strain localization to occur for low stress triaxialities (Figure 5 a)). From Figure 5 a), b) and c) it can be observed that the void softening in shear has a rather strong influence for the low stress triaxiality regime while this influence fades away and even deteriorates the predictions at large stress triaxialities. As suggested by Nielsen and Tvergaard (2010), this could be improved by balancing the contribution of the void softening in shear above a given stress triaxiality

threshold, but this modification is not included in the present work. According to Figure 5, setting  $k_s$  equal to 1 seems to be an appropriate choice to correlate with the unit cell simulations of Dunand and Mohr (2014) even though discrepancies are always larger around generalized compression ( $L = 1$ ). In contrast, the regime around generalized tension ( $L = -1$ ) seems to be well reproduced.

Failure loci are usually depicted as failure strain  $\varepsilon_f$  versus stress triaxiality  $T$  and Lode parameter  $L$ , but it is also interesting to transform the failure loci into stress space. Several stress quantities can be used to display a failure locus, e.g. the shear stress versus normal stress (Dunand and Mohr 2014), the major principal stress versus stress triaxiality (Di et al 2016) or the principal stresses, which are selected herein. We recall that the stress states emphasized here pertain to the material outside the band. Figure 6 shows the failure loci obtained with different shear parameters  $k_s$  in the principal stress plane. The isotropy of the constitutive model is utilized to visualize the entire failure locus from the data obtained in the Lode angle range  $\theta_L = 0^\circ$  ( $L = -1$ ) to  $\theta_L = 60^\circ$  ( $L = 1$ ).

The stress-based failure loci presented in Figure 6 are covering the full range of stress triaxialities studied, i.e.,  $T$  varies from 0 to 4. It is interesting to note that the shapes of the stress-based failure locus are always similar, independent of the value of  $k_s$ . At low stress triaxiality, some kind of flower pattern is observed. The radius of the failure locus (the equivalent stress in this case) is decreasing when approaching generalized shear states ( $30^\circ$  in the figure) and increasing towards generalized tension and compression ( $0^\circ$  and  $60^\circ$ ). This phenomenon is directly linked to the evolution of the failure strain as a function of the Lode parameter  $L$  (Figure 5). When approaching generalized shear, the ductility is decreasing and thus the

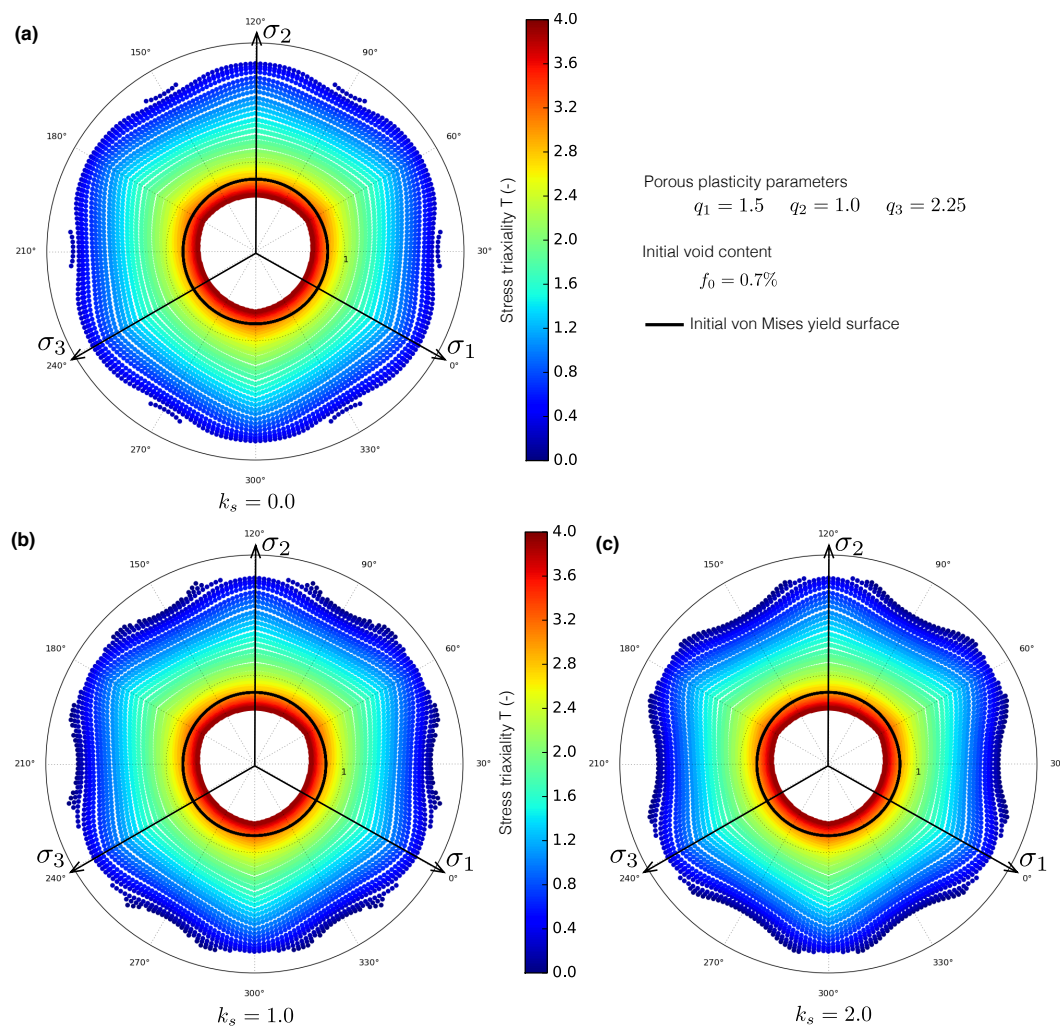


**Fig. 6** Effect of the void softening in shear on the failure locus in stress space: a)  $k_s = 0.0$ , b)  $k_s = 1.0$  and c)  $k_s = 2.0$ .

equivalent stress  $\sigma_{eq}$  at localization is lower than the one in generalized tension or compression because outside the band  $J_2$  plasticity is used and  $\sigma_{eq} = \sigma_M$ .

The flower-shaped failure locus is somewhat similar to yield and fracture surfaces recently proposed to account for the influence of the third invariant  $J_3$  on the behaviour of metals (Xue and Wierzbicki 2008; Chocron et al 2011). At higher

stress triaxiality with  $T$  ranging approximately between 0.8 and 2.0, a change in the shape of the failure locus takes place from the flower shape to a shape resembling the Tresca criterion. In this region, the modified Hosford-Coulomb criterion recently proposed by Mohr and Marcadet (2015) would be a suitable choice to describe the failure locus mathematically. When further increasing the stress triaxiality, the shape of the failure locus changes into a shape resembling the von Mises yield surface, thus indicating that macroscopic failure takes place just after yielding. When the hydrostatic stress applied to the band is about three times the yield stress of the material (corresponding to a stress triaxiality  $T = 3$  here) the failure locus is inside the yield surface. At very large stress triaxialities, the material inside the band experiences yielding, plastic deformation and localization while the material outside the band is still in the elastic domain. Accordingly, a transition from ductile failure to a macroscopic brittle failure is obtained in the presence of initial voids at large stress triaxialities. Note that, by introducing a small porosity outside the band, evidently smaller than the one inside, this transition from ductile to brittle fracture could be postponed to even higher stress triaxiality. In this study, brittle failure is defined as a phenomenon where plasticity, void growth and localization takes place in an infinitely small region while the surrounding material still behaves elastically. To some extent, this definition resembles the micro-plasticity phenomena used in high-cycle fatigue (Lemaitre and Desmorat 2005; Desmorat et al 2007).

#### 6.4 Effect of void nucleation

Voids in metals are supposed to be either present before any straining of the material, due to manufacturing processes, or to be nucleated during straining. Void nucleation could be caused by decohesion between hard particles and the matrix material or possibly between hard and soft phases. Another mechanism for void nucleation is particle cracking. To investigate the effect of void nucleation on failure by strain localization, the initial void content,  $f_0 = 0.7\%$ , is replaced by a similar volume fraction of void nucleating particles,  $f_n = 0.7\%$ . The void softening in shear is not included in the first results presented below. The effect of void nucleation on the failure locus is shown in Figure 7 a), where the failure strain  $\varepsilon_f$  is plotted against stress triaxiality  $T$  and Lode parameter  $L$ . The results from the unit cell simulations of Dunand and Mohr (2014) are included to get a reference for the magnitude of the failure strain. But it should be noted that a direct comparison is not possible here because the unit cell simulations were based on a preexisting void.

The shape of the failure locus is not markedly affected when one uses a localization analysis based either on initial porosity or void nucleation for stress triaxialities comprised between 0.2 and 1 (Figure 7 a)). However, the magnitude of the failure strain is affected, and the failure locus is shifted upwards by this change of mechanism. The parameters governing the void nucleation are given the following values: the mean equivalent plastic strain for nucleation  $p_n$  is taken to be equal to the equivalent plastic strain at diffuse necking under pure tension, and the associated standard deviation  $s_N$  is set to 0.1. As these parameters are difficult to estimate, even with access to experimental data, a sensitivity study

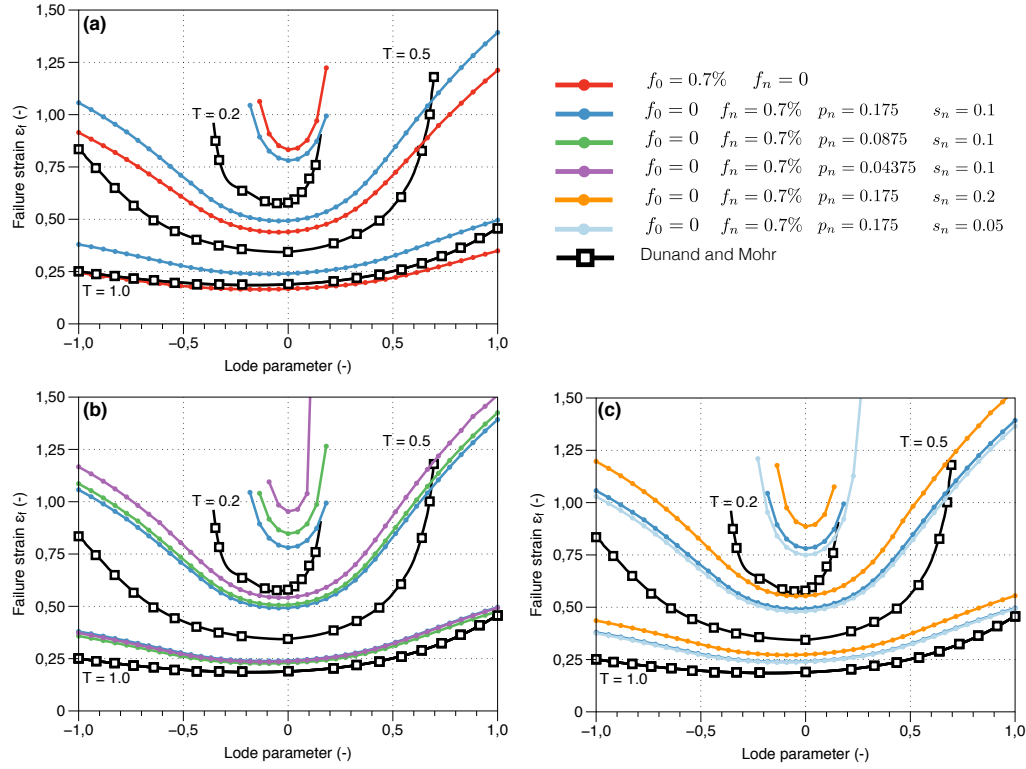


**Fig. 7** Effect of void nucleation on the failure locus: a) comparison between initial porosity and void nucleation, b) effect of the mean equivalent plastic strain for nucleation  $p_n$  and c) effect of the associated standard deviation  $s_n$ .

was performed. Figure 7 b) and c) show the effect on the failure strain of varying  $p_n$  and  $s_n$ , respectively. The reduction of  $p_n$  from 0.175, which is the strain to necking, to 0.04375, which is one-quarter of the strain to necking, has only a small effect on the failure locus for moderate stress triaxialities ( $T = 0.5$  and  $T = 1.0$ ). At the lowest stress triaxiality ( $T = 0.2$ ), the failure strain is more affected by  $p_n$ . A similar trend is seen for the standard deviation  $s_n$  in Figure 7 c), where  $s_n$  ranges from 0.05 to 0.2.

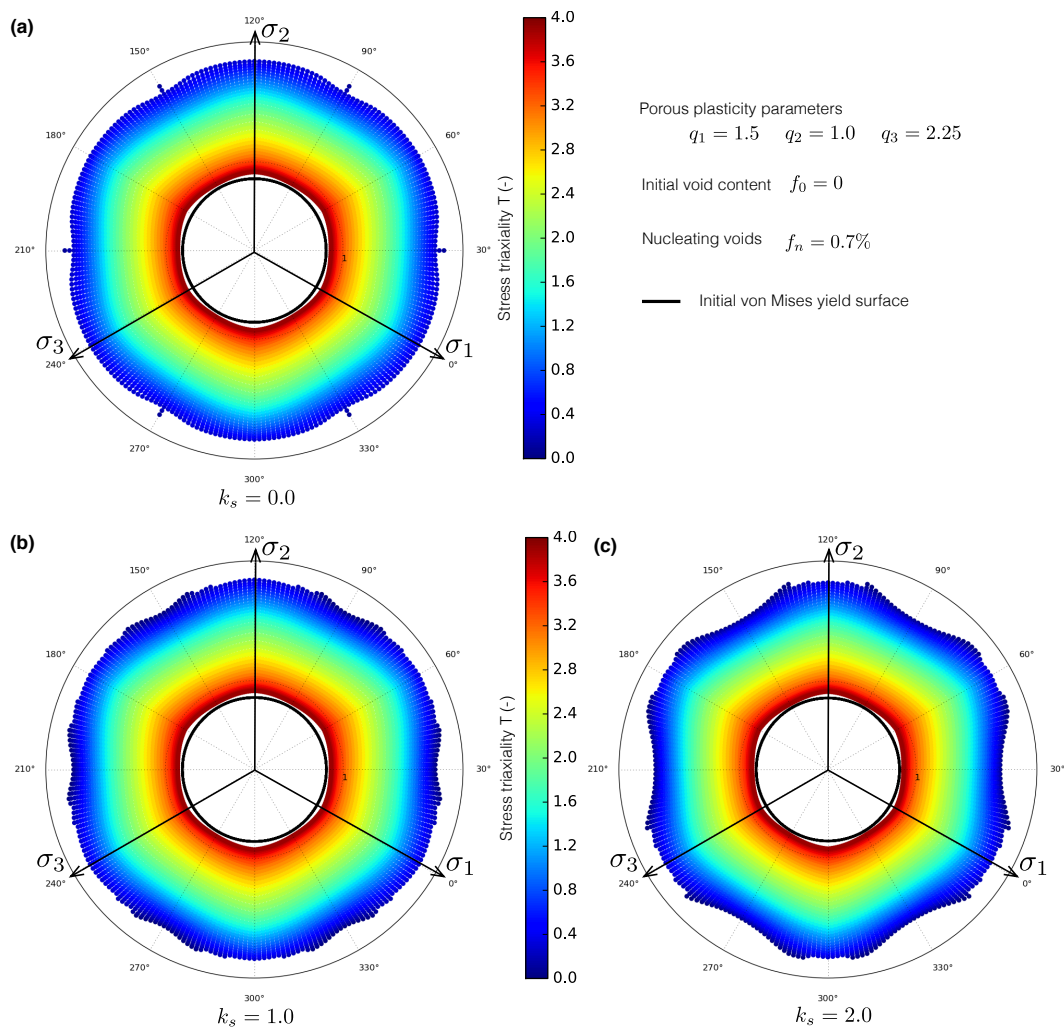


**Fig. 8** Effect of void softening in shear on the failure locus in stress space in the case of void nucleation: a)  $k_s = 0.0$ , b)  $k_s = 1.0$  and c)  $k_s = 2.0$ .

The effect of void softening in shear on failure when void nucleation is considered is illustrated in Figure 8 in terms of the failure loci on the deviatoric stress plane. The flower-shaped fracture loci for low stress triaxialities are seen also in this case, and again the shape of the fracture loci changes into a shape similar to the Tresca criterion with increasing stress triaxiality. The largest difference be-

tween the failure loci obtained when using localization analysis based either on initial porosity or void nucleation is found at very high stress triaxialities. The transition from ductile to brittle failure observed for the case with initial porosity is not found in the simulations with void nucleation. The reason for this is that the materials inside and outside the band yield simultaneously and then the porosity inside the band develops with plastic straining. This precludes localization inside the band while the material outside is elastic and the failure loci in the deviatoric stress plane will always be bounded from below by the yield locus.

## 7 Underlying mechanisms in the imperfection band analyses

### 7.1 Preamble

While Section 6 addressed the failure locus in terms of the equivalent plastic strain and the stress state in the material outside the band, this section deals with the evolution of the stress state inside the band. The aim is to investigate localization from the perspective of the band and thus substantiate the observations made in the simulations based on the imperfection analysis. In this section, the localization strain  $\varepsilon_l$  is defined as the equivalent plastic strain  $p$ , either inside the imperfection band or outside, when localization is detected into the voided material of the critical imperfection band or in the homogeneous material in the case of bifurcation analyses.

Two important points must be raised before presenting any result from this perspective. First, the adopted computational procedure utilizes a finite number of band orientations to evaluate strain localization. In this section, we only consider the band with the orientation leading to the lowest ductility for a given stress

state imposed outside the band. Second, when analysing the data extracted from within an imperfection band, it must be kept in mind that these results can be sensitive to the definition of localization. In the numerical simulations, loss of ellipticity is defined here as the first instant where the determinant of the acoustic tensor  $\mathbf{A}^t$  becomes negative, while the stringent condition for loss of ellipticity is  $\det \mathbf{A}^t = 0$ . By using sufficiently small strain increments  $\Delta \boldsymbol{\varepsilon}$ , the influence of this approximation on the predicted values of the quantities outside the band at localization can be made negligible. To this end, the norm of the strain increment  $\|\Delta \boldsymbol{\varepsilon}\|$  was set to  $10^{-5}$  in the above simulations. However, the incremental deformation non-uniformity  $\Delta \mathbf{q}$  cannot be controlled and its magnitude grows exponentially when approaching loss of ellipticity. Therefore, the final values of the equivalent plastic strain and the stress state in the localization band are somewhat difficult to get precisely. Obviously, the value of the equivalent plastic strain at localization inside the band will be an upper bound.

The results presented in the following are all obtained with the Gurson model using the porous plasticity parameters,  $q_1 = 1.5$ ,  $q_2 = 1.0$  and  $q_3 = q_1^2$ , the void softening in shear parameter  $k_s = 1.0$ , and either initial porosity  $f_0 = 0.007$  or void nucleation set by  $f_n = 0.007$   $p_n = 0.175$  and  $s_n = 0.1$ .

## 7.2 Evolution of the local states inside the localization band

The evolution of the equivalent stress  $\sigma_{eq}$  and hydrostatic stress  $\sigma_h = \frac{1}{3} \boldsymbol{\sigma} : \mathbf{I}$  (inside and outside the band) as a function of the equivalent plastic strain  $p$  (respectively inside and outside the band) for a selection of stress states is shown in Figure 9. Subfigures a) and b) present these results for an analysis with initial porosity, while

the results in subfigures c) and d) concern an analysis with void nucleation. The results are presented for stress states outside the band defined by stress triaxiality  $T = 0.5, 1.0$  and  $2.0$  and Lode parameter  $L$  equal to  $0$ .

For both the considered cases, the equivalent and hydrostatic stresses inside the band are following those outside the band until void growth starts to compete with the work hardening and eventually leads to softening. An exception is seen in the simulation using initial porosity and a stress triaxiality equal to  $2$ , for which the material inside the band yields well before yielding takes place outside, and thus the two curves differ from the start. Also, the hydrostatic stress differs inside and outside the band, indicating a change in the stress state within the band. This will be discussed in more detail later on. Finally, Figure 9 shows that the equivalent plastic strain is always greater inside the band than outside due to the porosity evolution and ensuing strain softening within the imperfection band. The strain outside the band at localization is represented by colored circles in Figure 9.

The evolution of the porosity inside the critical band as a function of the equivalent plastic strain outside the band is given in Figure 10 a) and b) for analyses with initial porosity and void nucleation, respectively. It is seen that the porosity grows exponentially when approaching localization, but for both cases the final porosity is quite low at localization (around  $6\%$  for the largest ductility presented here). For moderate stress triaxialities, the porosity evolution and the final value of the porosity in the band are found to be similar in the two cases. This agrees with the observation made in Section 6 that using either initial porosity or void nucleation has only minor effects of the failure strain for moderate stress triaxiality.

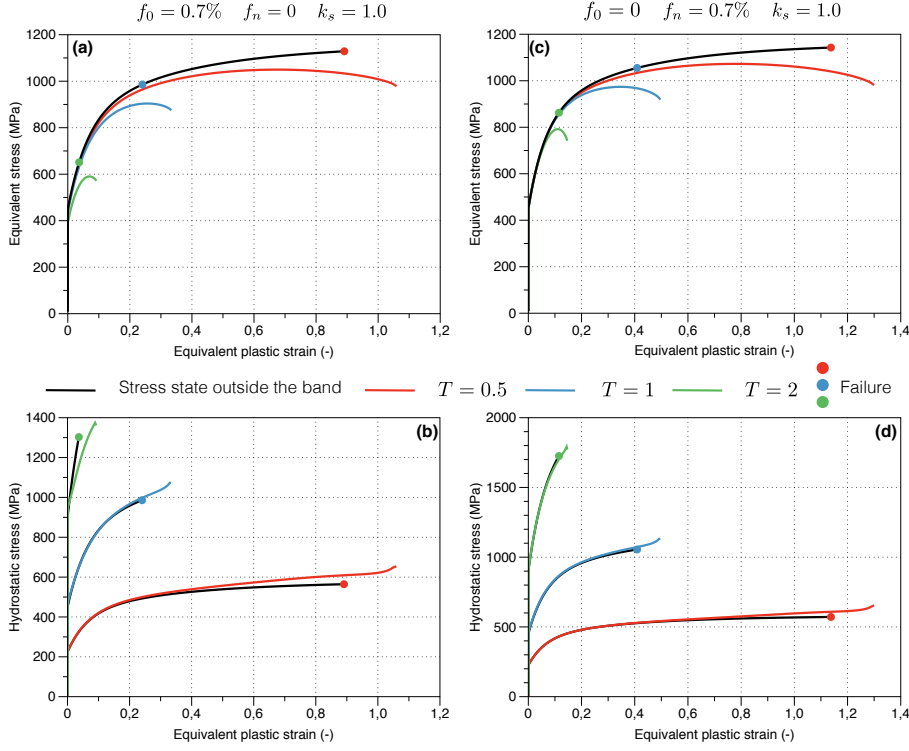


**Fig. 9** Evolution of the equivalent stress  $\sigma_{eq}$  and hydrostatic stress  $\sigma_h$  inside and outside the localization band with the associated equivalent plastic strain  $p$  for the case of initial porosity and void nucleation. Note that the data extracted from the imperfection band are plotted as function of the equivalent plastic strain developed inside the band.

Figure 11 a) and b) present the evolution of the normalized determinant  $\xi_{\mathbf{A}}$  of the acoustic tensor and the strain jump parameter  $\xi_{\Delta\epsilon}$  as a function of the equivalent plastic strain outside the band for analyses considering either an initial porosity or void nucleation, respectively. The normalized determinant of the acoustic tensor  $\xi_{\mathbf{A}}$  and the strain jump parameter  $\xi_{\Delta\epsilon}$  are defined as

$$\xi_{\mathbf{A}} = \frac{\det \mathbf{A}^t}{\det \mathbf{A}}, \quad \xi_{\Delta\epsilon} = \frac{\sqrt{\Delta\epsilon_b : \Delta\epsilon_b}}{\sqrt{\Delta\epsilon : \Delta\epsilon}} \quad (40)$$

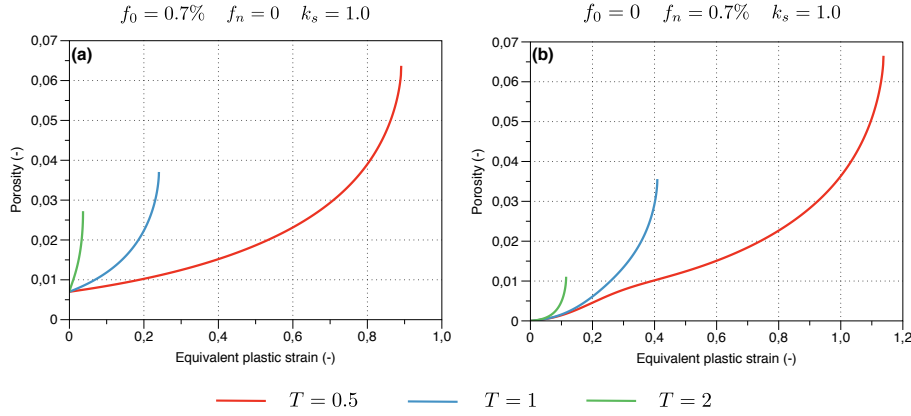


**Fig. 10** Evolution of the porosity in the critical band against equivalent plastic strain outside the band: a) initial porosity and b) void nucleation.

where  $\mathbf{A} = \mathbf{n} \cdot \mathbf{C} \cdot \mathbf{n}$  is the acoustic tensor of the elastic material. There are only minor differences found between the two cases shown in Figure 11 a) and b). While the normalized determinant of the acoustic tensor  $\xi_{\mathbf{A}}$  is gradually decreasing towards zero, the strain jump parameter  $\xi_{\Delta\epsilon}$  is rather constant and almost equal to unity until exponential growth occurs in the vicinity of loss of ellipticity. Considering only the evolution of the determinant of the acoustic tensor would lead to the conclusion that strain localization is a progressive phenomenon. But the evolution of the strain jump parameter shows that the localization of deformation in the band is abrupt.

Figure 12 a) and b) present the initial and final orientations  $\phi_0$  and  $\phi_f$  of the critical band for the two types of simulations where initial porosity and void nucleation are considered, respectively. The final orientation is obtained at the time of failure  $t_f$ . The band orientations are shown for stress triaxiality  $T \in [0, 4]$  and Lode parameter  $L$  equal to -1 (i.e., generalized tension) outside the band. The complementary angle  $\alpha$ , which is defined by  $\cos \alpha = \dot{\mathbf{q}} \cdot \mathbf{n}$ , defines the localization

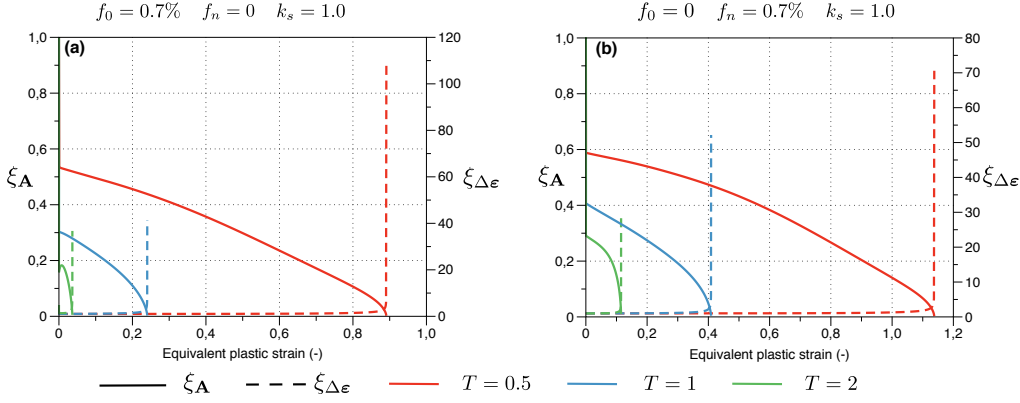


**Fig. 11** Evolution of the normalized determinant of the acoustic tensor  $\xi_A$  and the strain jump parameter  $\xi_{\Delta\varepsilon}$  with the equivalent plastic strain  $p$  outside the band: a) initial porosity and b) void nucleation.

mode, e.g., if it is a shear band ( $\alpha = 90^\circ$ ) or a dilatation band ( $\alpha = 0^\circ$ ). The final value of the complementary angle  $\alpha_f = \alpha(t_f)$  is also plotted in the figures. The definitions of the angles  $\phi$ ,  $\phi_0$  and  $\alpha$  are given in Figure 12 c). It is easily seen that the critical band experiences large rotation for moderate stress triaxiality, while for large stress triaxiality (say, above 2) localization occurs rapidly and the band does not rotate. Using initial porosity or void nucleation in the simulations has a strong influence on the critical band orientation. In the case of initial porosity, the critical localization mode is a shear-dominated band with  $\phi_f \approx 45^\circ$  ( $\alpha_f \approx 85^\circ$ ) for low stress triaxiality and then it turns gradually into a dilatation-dominated band with  $\phi_f \approx 0^\circ$  ( $\alpha_f \approx 0^\circ$ ) with increasing stress triaxiality. In the case of void nucleation, the critical band retains its shear band character for the whole range of stress triaxiality, and  $\phi_f$  varies between  $35^\circ$  and  $45^\circ$ .

As shown in Figure 9, the stress state inside the localization band is initially similar to the one imposed outside the band, but starts to drift away when void

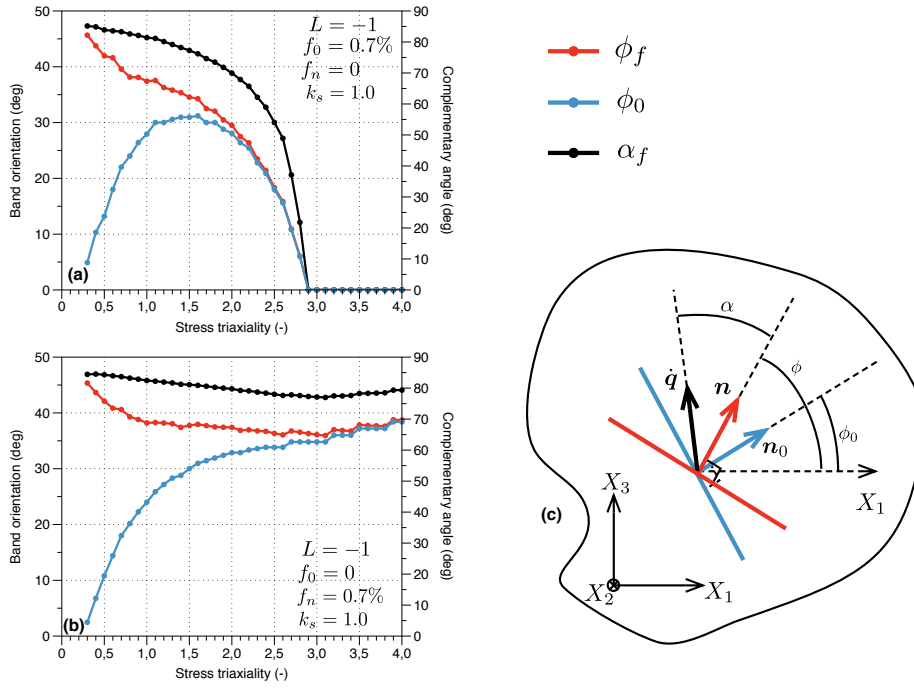


**Fig. 12** Band orientations  $\phi_0$  and  $\phi_f$  and the complementary angle  $\alpha_f$  as functions of stress triaxiality ( $L = -1$ ): a) initial porosity, b) void nucleation and c) definitions of the angles.

growth takes place. Figure 13 a) and b) show the stress path inside the band in terms of stress triaxiality  $T$  and Lode parameter  $L$  for an imposed stress triaxiality of 0.5 and various Lode parameters (from -1 to 1) outside the band. Even if proportional loading is maintained outside the band during the entire loading process (indicated by the black dots in Figure 13), a strongly non-proportional stress history is observed inside the bands. In these simulations, the stress state inside the band in the vicinity of loss of ellipticity is always rather close to generalized shear ( $L = 0$ ), even when the Lode parameter imposed outside the band is equal to -1 or 1.

The observation that the localization occurs in the vicinity of generalized shear for moderate stress triaxiality is interesting and could be used to explain the shape of the failure locus obtained by Dunand and Mohr (2014). For a stress triaxiality of 0.5, the minimum ductility is found to be close to generalized shear ( $L = 0$ ), in both the unit cell analyses and the imperfection analyses, while larger ductility is found for generalized tension ( $L = -1$ ) and generalized compression ( $L = 1$ ). The ductility is found to be larger in generalized compression than in generalized tension. These observations can be explained from Figure 13a). When the Lode parameter outside the band is equal or close to zero, the conditions are favourable for localization of deformation into a shear band and as a result, the macroscopic ductility is at the lowest. In contrast, if the material is subjected to generalized tension or generalized compression, the localization band must be subjected to significant straining before its stress state drifts towards generalized shear, thus increasing the macroscopic ductility. One simple way to explain the asymmetry in ductility between generalized tension and generalized compression is to consider the evolution of the stress triaxiality inside the localization band. According to Figure 13 a) and b), the stress triaxiality increases inside the localization band when the material outside the band is subjected to generalized tension, while it decreases if generalized compression is applied outside the band. Accordingly, the void growth will be faster when generalized tension is applied outside the band due to the increased hydrostatic stress and the result is a lower ductility than in generalized compression.

At large stress triaxialities, the evolution of the stress state in terms of Lode parameter  $L$  and stress triaxiality  $T$  inside the imperfection bands for initial porosity and void nucleation are given in Figure 14 a) and b), respectively. In the case of

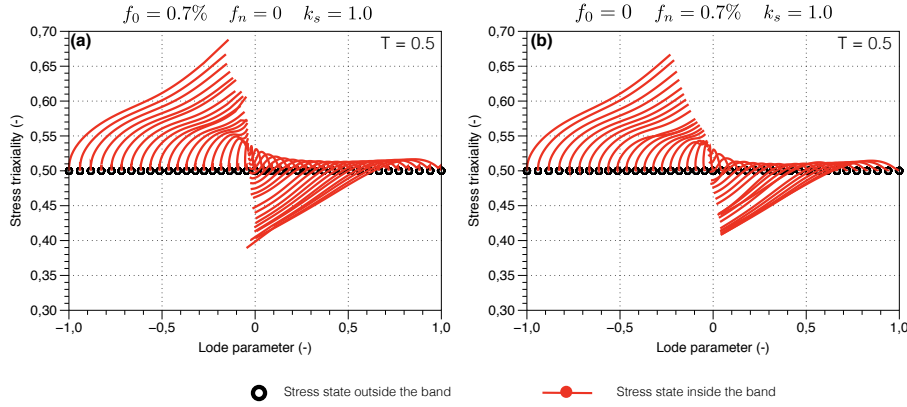


**Fig. 13** Evolution of the stress states inside the localization bands in simulations with  $T = 0.5$  and a) initial porosity or b) void nucleation.

an initially voided material (Figure 14 a)) with stress triaxiality outside the band fixed to 4, the imperfection bands still exhibit a strongly non-proportional load path and localization always occurs around generalized tension. Accordingly, the macroscopic failure locus at this level of stress triaxiality will find its minimum in generalized tension. At large stress triaxialities, the initially voided imperfection bands tend to localize into a dilational mode (Figure 12 a)). The dilatation mode is favoured by generalized tension in contrast to shear banding which is favored by generalized shear. When the imperfection bands consist of a void-nucleating material, their local stress states are drifting from the one imposed outside the bands towards generalized shear (Figure 12 b)) but never reach it, except when a small Lode parameter is imposed outside the band. The full range of stress states imposed outside the bands (regularly spaced black dots) and the resulting stress states inside the bands (red circles) *at strain localization* are presented in Figure 15 a) and b) for simulations using initial porosity or void nucleation, respectively. In the case of initial porosity, the stress state at localization changes gradually from

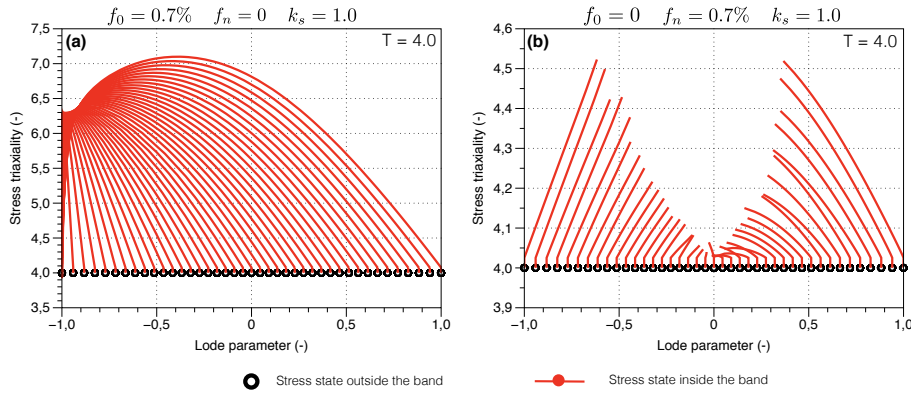


**Fig. 14** Evolution of the stress states inside the localization bands in simulations with  $T = 4$  and a) initial porosity or b) void nucleation.

generalized shear for low triaxiality towards generalized tension for high triaxiality. Simultaneously, the localization mode changes from a shear band to a dilatation band (cf. Figure 12 a)), and at the highest triaxiality localization occurs before yielding takes place outside the band. In the case of void nucleation, the stress state is close to generalized shear for low triaxiality, while at higher triaxiality the Lode parameter at localization is between -0.5 and 0.5. The localization mode is a shear-dominated band even at high triaxiality (cf. Figure 12 b)). A much larger spread of the stress state inside the band at localization is obtained when void nucleation is used rather than initial porosity (Figure 15 b)).

### 7.3 Comparison between bifurcation and imperfection analyses

In this section, bifurcation analyses are carried out with the parameters of the Gurson model used in the imperfection analyses of the previous section. The stress triaxiality and Lode parameter are both constant until loss of ellipticity occurs.

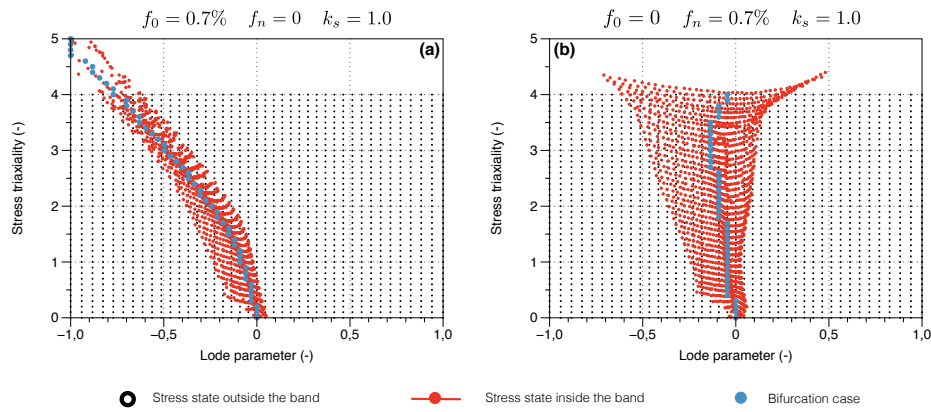


**Fig. 15** Full range of stress states imposed outside the bands (regularly spaced black dots) and resulting stress states inside the bands (red circles) at failure: a) initial porosity and b) void nucleation.

Simulations are performed using either initial porosity or void nucleation over a wide range of stress states.

The localization strains  $\varepsilon_l$  obtained for four different values of stress triaxiality ( $T = 0.5, 1.0, 2.0, 3.0$ ) as a function of the Lode parameter  $L$  are presented in Figure 16 a) and c) for the initially voided and void nucleating materials respectively. Note that a semi-log plot is used so that the small variation at large stress triaxialities can still be observed in the figure. The results obtained with the bifurcation analysis show similar trends as those found with the imperfection analysis: the ductility decreases with increasing stress triaxiality and the Lode dependence is strong. It is notable that the minimum ductility at a given stress triaxiality is not necessarily found at  $L = 0$ . In simulations using an initial porosity, the minimum ductility is located near  $L = 0$  for low stress triaxialities ( $T < 1.0$ ), while at larger stress triaxialities the point of minimum ductility drifts away from generalized shear towards generalized tension. For instance, at  $T = 3$  the minimum ductility

is obtained for a Lode parameter of -0.5 (Figure 16 a)). When void nucleation is adopted in the simulations (Figure 16 b)), the point of minimum ductility remains closer to generalized shear even if some deviations are observed. Moreover, it is important to notice that in contrast to the imperfection analysis, localization is difficult to obtain for positive values of the Lode parameter in the investigated range of strain. Figures 16 b) and d) present the material softening indicator  $H_s$

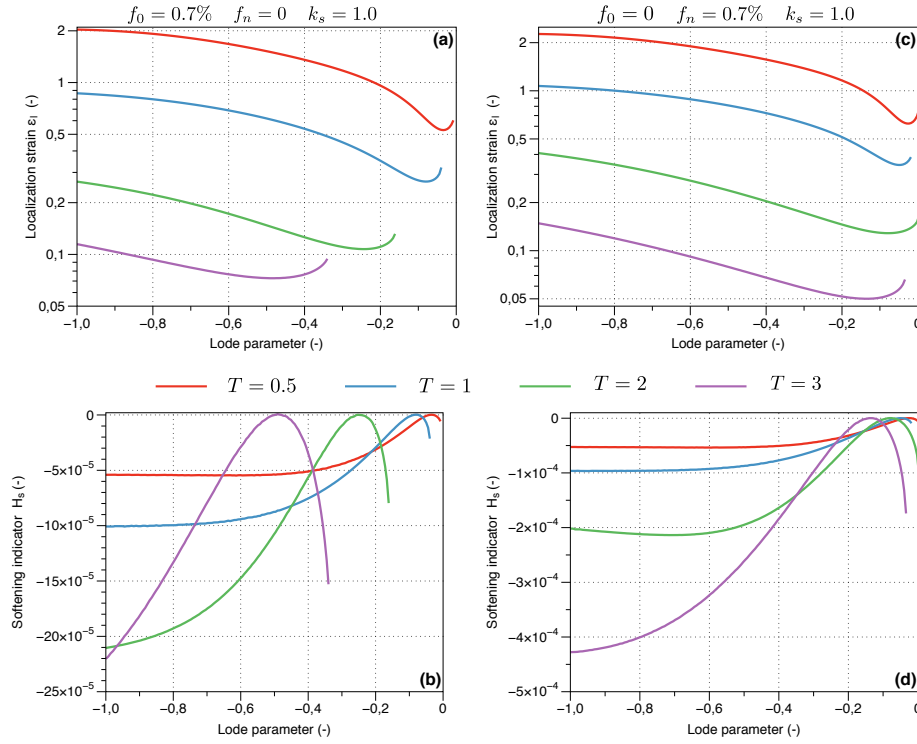


**Fig. 16** Localization strain  $\epsilon_l$  and material softening indicator  $H_s$  as function of the Lode parameter  $L$  obtained with the bifurcation analyses of the band material: a) and b) initial porosity, c) and d) void nucleation.

required to get a bifurcation in the porous materials with initial voids and void

nucleation. The material softening indicator  $H_s$  is defined as

$$H_s \equiv -d\Phi|_{\sigma=const} = -\left(\frac{\partial\Phi}{\partial\sigma_M}d\sigma_M + \frac{\partial\Phi}{\partial f}df\right) \quad (41)$$

where  $H_s$  is positive for strain hardening and negative for strain softening. It is noted that, according to Figure 16 b) and d), the point of minimum ductility at a given stress triaxiality corresponds to the maximum value of  $H_s$  which allows a bifurcation to occur and therefore the least amount of softening.

Figure 15 a) and b) compare the stress states at localization obtained with the imperfection and bifurcation analyses. The blue dots illustrate the locations in the stress space (defined by  $T$  and  $L$ ) of the points of minimum ductility in the bifurcation analyses, i.e., each point gives the Lode parameter  $L$  at which the minimum ductility is obtained at a given stress triaxiality  $T$ . As an example, for simulations with an initially voided material, the minimum ductility for a stress triaxiality of 3 is found for a Lode parameter equal to -0.5 in Figure 16a), and a blue circle is then present in Figure 15a) at the same location. It appears from Figure 15 that the stress state inside the localization band in an imperfection analysis is always close to the stress state giving the minimum ductility in the corresponding bifurcation analysis. This observation can be explained by the fact that loss of ellipticity can be reached for a smaller amount of material softening in these stress states (Figure 16). To investigate the potential reasons for the spread in the stress states of the imperfection bands at localization (Figure 15) a serie of bifurcation analyses is carried out. These dedicated bifurcation analyses are performed as follows:

- The imperfection analyses of Section 7.2 where the Lode parameter outside the band is fixed to  $L = 0$  or  $L = -1$  are selected.

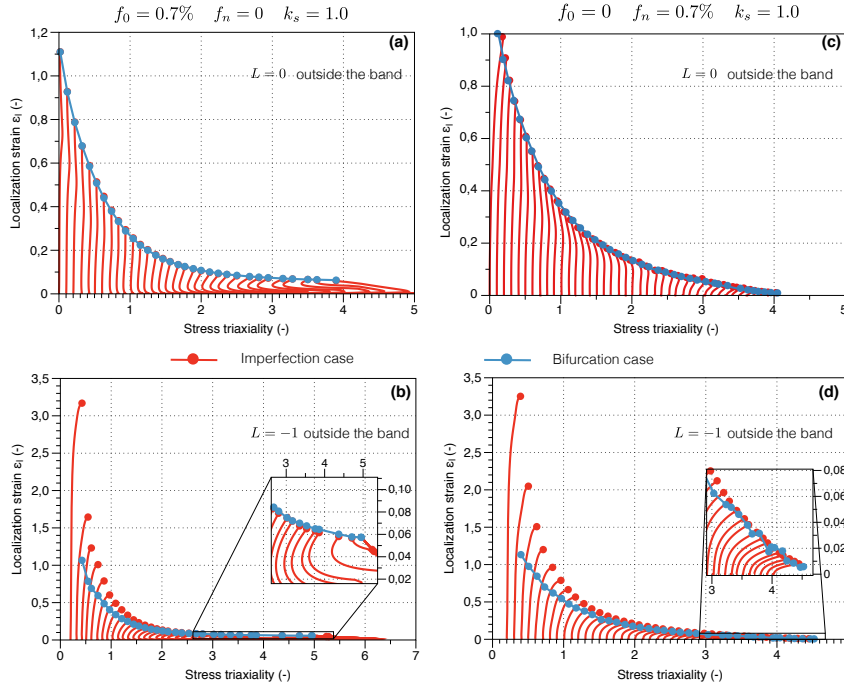


**Fig. 17** Comparison between the localization strain  $\varepsilon_l$  obtained with the imperfection and bifurcation methods for  $L = 0$  and  $-1$  outside the imperfection band: a) and b) with initial porosity, c) and d) with void nucleating.

- The stress states at localization of the imperfection bands are extracted.
- Bifurcation analyses are carried out under proportional loadings for these particular stress states.
- The localization strain  $\varepsilon_l$  is extracted from the bifurcation analyses when loss of ellipticity is reached and compared to the localization strain reached in the bands of the imperfection analyses.

Figure 17 presents the localization strains obtained for the initially voided and void nucleating materials, respectively, when the Lode parameter outside the imperfection band is fixed to  $L = 0$  and  $L = -1$ . A rather good correlation is found

between the localization strains as long as the loading is proportional or slightly non-proportional. When the loading is strongly non-proportional like for low stress triaxiality and  $L = -1$  outside the band, a large difference is observed between the localization strains  $\varepsilon_l$  obtained with the imperfection and bifurcation analyses. Recall here that a large variation in the Lode parameter of the imperfection bands is observed at low stress triaxiality for axisymmetric stress states (Figure 13), because localization occurs for stress states near generalized shear.

Based on the present results, it appears that the spread in the stress state inside the imperfection bands at localization (Figure 15) is linked to the degree of non-proportionality of the loading. When the loading is nearly proportional the stress state inside the band is located near a point of minimum ductility of the bifurcation analyses. In the case of strongly non-proportional loading inside the imperfection bands, loss of ellipticity might occur before the bands have reached a state giving minimum ductility in the bifurcation analyses.

### Concluding remarks

Strain localization is used here to describe ductile failure and investigated in this study by employing the imperfection analysis proposed by Rice (1976). An important ingredient in the imperfection analysis is the inelastic mechanism used in the imperfection band to trigger the localization process. The Gurson porous plasticity model is used here with some of its extensions, namely the Tvergaard parameters (Tvergaard 1981), the shear modification proposed by Nahshon and Hutchinson (2008), and using either initial porosity or void nucleation. The results obtained with the strain localization analyses (using the imperfection approach)

are compared with the 3D unit cell simulations reported by Dunand and Mohr (2014). It is shown that the imperfection analysis provides qualitatively similar results as the full 3D unit cell simulations reported by Dunand and Mohr (2014), while having a significantly lower computational cost.

When using the imperfection analyses to study ductile failure, from the perspective of *the material outside the band*, the following conclusions are found:

- The shapes of the failure loci appear unaffected by the Tvergaard parameters  $(q_1, q_2, q_3)$  while the failure strain levels are markedly affected.
- The shapes of the failure loci in stress space show strong variations from low to high stress triaxialities.
- The voiding mechanism (initial or nucleating porosities) does not seem to have a large influence in the moderate stress triaxiality regime.
- At large stress triaxialities in the presence of initial porosity, a macroscopic transition from ductile to brittle failure is observed.

When studying the imperfection analyses from the perspective of *the material inside the band*, the following conclusions are drawn:

- The evolution of the stress triaxiality and the Lode parameter inside the imperfection bands can be used to explain the shape of the failure locus.
- When increasing the stress triaxiality, it is found that the stress states inside the initially voided bands are drifting from generalized shear towards generalized tension. This correlates with the transition from shear banding to dilatational banding.

- The void-nucleating imperfection bands do not exhibit such transition and at localization their stress states are always shifting towards generalized shear and their deformation modes are always shear-dominated.
- The brittle failure phenomenon observed in the presence of an initial porosity is linked to the early yielding of the material inside the band as a result of the high stress triaxiality imposed by the material outside the band.

In an attempt to understand the underlying mechanisms of the imperfection approach, bifurcation analyses were carried out on the porous material of the imperfection bands. The following conclusions are drawn:

- When the loading inside the imperfection band is nearly proportional, a good correlation with the point of minimum ductility predicted by the bifurcation analyses is obtained.
- When the loading inside the imperfection band is strongly non-proportional, the stress state inside the imperfection bands is drifting towards the point of minimum ductility of the bifurcation analyses but localization occurs before reaching this state.

While the obtained results show that the imperfection analyses can be used to obtain a qualitative understanding of ductile failure, quantitative estimates of the ductility of metals are difficult to obtain at low stress triaxiality. It is believed though that a quantitative estimate could be reached by employing a more advanced porous plasticity model (Madou and Leblond 2012; Morin et al 2016). Current investigations also show that the approach is able to predict failure characteristics for materials with complex microstructures without taking into account this complexity. Another point of interest is the description of ductile

failure under non-proportional loadings, where the imperfection band approach could also be used.

**Acknowledgements** O.S.H. and D.M. would like to acknowledge the financial support from the Centre for Advanced Structural Analysis (CASA) (Project No. 237885) as well as the FractAl project (Project No. 250553) funded by the Research Council of Norway and NTNU. Part of this work was performed when A.B. was a guest of the Structural Impact Laboratory at the Department of Structural Engineering at NTNU. A.B. also gratefully acknowledges the FractAl project for the financial support during his stay in Trondheim.

## References

- Aravas N (1987) On the numerical integration of a class of pressure dependent plasticity models. *International Journal for Numerical Methods in* 24:1395–1416, DOI 10.1002/nme.1620240713
- Bai Y, Wierzbicki T (2010) Application of extended Mohr-Coulomb criterion to ductile fracture. *International Journal of Fracture* 161(1):1–20, DOI 10.1007/s10704-009-9422-8
- Bao Y, Wierzbicki T (2004) On fracture locus in the equivalent strain and stress triaxiality space. *International Journal of Mechanical Sciences* 46(1):81–98, DOI 10.1016/j.ijmecsci.2004.02.006
- Barsoum I, Faleskog J (2007) Rupture mechanisms in combined tension and shear-Micromechanics. *International Journal of Solids and Structures* 44(17):5481–5498, DOI 10.1016/j.ijsolstr.2007.01.010
- Barsoum I, Faleskog J (2011) Micromechanical analysis on the influence of the Lode parameter on void growth and coalescence. *International Journal of Solids and Structures* 48(6):925–938, DOI 10.1016/j.ijsolstr.2010.11.028
- Basu S, Benzerga AA (2015) On the path-dependence of the fracture locus in ductile materials: Experiments. *International Journal of Solids and Structures* 71:79–90, DOI 10.1016/j.ijsolstr.2015.06.003

- Benallal A (2017) Constitutive equations for porous solids with matrix behaviour dependent on the second and third stress invariants. *International Journal of Impact Engineering* 000:1–16, DOI 10.1016/j.ijimpeng.2017.05.004, URL <http://linkinghub.elsevier.com/retrieve/pii/S0734743X17301033>
- Benallal A, Comi C (1996) Localization analysis via a geometrical method. *International Journal of Solids and Structures* 33(1):99–119, DOI 10.1016/0020-7683(95)00018-6
- Benzerga A, Surovik D, Keralavarma S (2012) On the path-dependence of the fracture locus in ductile materials Analysis. *International Journal of Plasticity* 37:157–170, DOI 10.1016/j.ijplas.2012.05.003
- Besson J, Steglich D, Brocks W (2001) Modeling of crack growth in round bars and plane strain specimens. *International Journal of Solids and Structures* 38(46-47):8259–8284, DOI 10.1016/S0020-7683(01)00167-6
- Bryhni Dæhli LE, Børvik T, Hopperstad OS (2016) Influence of loading path on ductile fracture of tensile specimens made from aluminium alloys. *International Journal of Solids and Structures* 88-89:17–34, DOI 10.1016/j.ijsolstr.2016.03.028
- Chalal H, Abed-Meraim F (2015) Hardening effects on strain localization predictions in porous ductile materials using the bifurcation approach. *Mechanics of Materials* 91, Part 1:152–166, DOI <http://dx.doi.org/10.1016/j.mechmat.2015.07.012>
- Chocron S, Erice B, Anderson CE (2011) A new plasticity and failure model for ballistic application. *International Journal of Impact Engineering* 38(8-9):755–764, DOI 10.1016/j.ijimpeng.2011.03.006
- Chu CC, Needleman A (1980) Void Nucleation Effects in Biaxially Stretched Sheets. *Journal of Engineering Materials and Technology* 102(3):249, DOI 10.1115/1.3224807
- Desmorat R, Kane A, Seyedi M, Sermage J (2007) Two scale damage model and related numerical issues for thermo-mechanical High Cycle Fatigue. *European Journal of Mechanics - A/Solids* 26(6):909–935, DOI 10.1016/j.euromechsol.2007.01.002
- Di Y, Lixun C, Chen B (2016) A New Fracture Criterion for Ductile Materials Based on a Finite Element Aided Testing Method. *Materials Science and Engineering: A* DOI 10.1016/j.msea.2016.06.076

- Dunand M, Mohr D (2014) Effect of Lode parameter on plastic flow localization after proportional loading at low stress triaxialities. *Journal of the Mechanics and Physics of Solids* 66(1):133–153, DOI 10.1016/j.jmps.2014.01.008
- Faleskog J, Gao X, Shih CF (1998) Cell model for nonlinear fracture analysis- I- Micromechanics calibration. *International Journal of Fracture* 89(4):355–373, DOI 10.1023/A:1007421420901
- Ghahremaninezhad A, Ravi-Chandar K (2013) Ductile failure behavior of polycrystalline Al 6061-T6 under shear dominant loading. *International Journal of Fracture* 180(1):23–39, DOI 10.1007/s10704-012-9793-0, URL <http://link.springer.com/10.1007/s10704-012-9793-0>
- Gruben G, Fagerholt E, Hopperstad OS, Børvik T (2011) Fracture characteristics of a cold-rolled dual-phase steel. *European Journal of Mechanics, A/Solids* 30(3):204–218, DOI 10.1016/j.euromechsol.2011.01.004
- Gruben G, Vysochinskiy D, Coudert T, Reyes A, Lademo OG (2013) Determination of ductile fracture parameters of a dual-phase steel by optical measurements. *Strain* 49(3):221–232, DOI 10.1111/str.12030
- Gruben G, Morin D, Langseth M, Hopperstad O (2017) Strain localization and ductile fracture in advanced high-strength steel sheets. *European Journal of Mechanics - A/Solids* 61:315–329, DOI 10.1016/j.euromechsol.2016.09.014
- Gurson A (1977) Continuum Theory of Ductile Rupture by Void Nucleation and Growth: Part I Yield Criteria and Flow Rules for Porous Ductile Media. *Journal of Engineering Materials and Technology* 99(1):2–15, DOI 10.1115/1.344340
- Haddag B, Abed-Meraim F, Balan T (2009) Strain localization analysis using a large deformation anisotropic elastic-plastic model coupled with damage. *International Journal of Plasticity* 25(10):1970–1996, DOI 10.1016/j.ijplas.2008.12.013
- Haltom S, Kyriakides S, Ravi-Chandar K (2013) Ductile failure under combined shear and tension. *International Journal of Solids and Structures* 50(10):1507–1522, DOI 10.1016/j.ijsolstr.2012.12.009, URL <http://dx.doi.org/10.1016/j.ijsolstr.2012.12.009> <http://linkinghub.elsevier.com/retrieve/pii/S0020768312005203>

- Hutchinson J, Tvergaard V (1981) Shear band formation in plane strain. DOI 10.1016/0020-7683(81)90053-6
- Jia Y, Bai Y (2016) Ductile fracture prediction for metal sheets using all-strain-based anisotropic eMMC model. *International Journal of Mechanical Sciences* DOI 10.1016/j.ijmecsci.2016.07.022
- Lemaitre J, Desmorat R (2005) *Engineering damage mechanics: Ductile, creep, fatigue and brittle failures*. Springer-Verlag, Berlin/Heidelberg, DOI 10.1007/b138882, arXiv:1011.1669v3
- Madou K, Leblond JB (2012) A Gurson-type criterion for porous ductile solids containing arbitrary ellipsoidal voids I: Limit-analysis of some representative cell. *Journal of the Mechanics and Physics of Solids* 60(5):1020–1036, DOI 10.1016/j.jmps.2011.11.008
- Marciniak Z, Kuczynski K (1967) Limit strains in the processes of stretch-forming sheet metal. *International Journal of Mechanical Sciences* 9(9):609 – 620, DOI 10.1016/0020-7403(67)90066-5
- Mear ME, Hutchinson JW (1985) Influence of yield surface curvature on flow localization in dilatant plasticity. DOI 10.1016/0167-6636(85)90035-3
- Mohr D, Marcadet SJ (2015) Micromechanically-motivated phenomenological Hosford-Coulomb model for predicting ductile fracture initiation at low stress triaxialities. *International Journal of Solids and Structures* 67-68:40–55, DOI 10.1016/j.ijsolstr.2015.02.024
- Morin L, Leblond Jb, Tvergaard V (2016) Application of a model of plastic porous materials including void shape effects to the prediction of ductile failure under shear-dominated loadings. *Journal of the Mechanics and Physics of Solids* 94:148–166, DOI 10.1016/j.jmps.2016.04.032
- Nahshon K, Hutchinson JW (2008) Modification of the Gurson Model for shear failure. *European Journal of Mechanics, A/Solids* 27(1):1–17, DOI 10.1016/j.euromechsol.2007.08.002
- Needleman a, Rice JR (1979) Limits to ductility set by plastic flow localization
- Nielsen KL, Tvergaard V (2010) Ductile shear failure or plug failure of spot welds modelled by modified Gurson model. *Engineering Fracture Mechanics* 77(7):1031–1047, DOI 10.1016/j.engfracmech.2010.02.031
- Papasidero J, Doquet V, Mohr D (2014) Determination of the Effect of Stress State on the Onset of Ductile Fracture Through Tension-Torsion Experiments.

- 
- Experimental Mechanics 54(2):137–151, DOI 10.1007/s11340-013-9788-4, URL <http://link.springer.com/10.1007/s11340-013-9788-4>
- Rice JR (1976) The localization of plastic deformation. In: In: 14th International Congress of Theoretical and Applied Mechanics,, pp 207–220
- Roth CC, Mohr D (2015) Ductile fracture experiments with locally proportional loading histories. International Journal of Plasticity 79:328–354, DOI 10.1016/j.ijplas.2015.08.004
- Rudnicki JW, Rice JR (1975) Conditions for the localization of deformation in pressure-sensitive dilatant materials. Journal of the Mechanics and Physics of Solids 23(6):371–394, DOI 10.1016/0022-5096(75)90001-0
- Saje M, Pan J, Needleman A (1982) Void nucleation effects on shear localization in porous plastic solids. International Journal of Fracture 19(3):163–182, DOI 10.1007/BF00017128
- Tvergaard V (1981) Influence of voids on shear band instabilities under plane strain conditions. International Journal of Fracture 17(4):389–407, DOI 10.1007/BF00036191
- Tvergaard V (2015) Study of localization in a void-sheet under stress states near pure shear. International Journal of Solids and Structures 75-76(August):134–142, DOI 10.1016/j.ijsolstr.2015.08.008
- Xue L, Wierzbicki T (2008) Ductile fracture initiation and propagation modeling using damage plasticity theory. Engineering Fracture Mechanics 75(11):3276–3293, DOI 10.1016/j.engfracmech.2007.08.012
- Yamamoto H (1978) Conditions for shear localization in the ductile fracture of void-containing materials. International Journal of Fracture 14(4):347–365, DOI 10.1007/BF00015989